APPLICATION OF MEMS-BASED INERTIAL GRAVIMETRY TO THE PLANETARY SCIENCES

An Undergraduate Research Scholars Thesis

by

CHANDLER S. LAWSON

Submitted to the LAUNCH: Undergraduate Research office at
Texas A&M University
in partial fulfillment of requirements for the designation as an

UNDERGRADUATE RESEARCH SCHOLAR

Approved by
Faculty Research Advisor: Dr. Michael E. Evans

May 2021

Major: Marine Sciences

RESEARCH COMPLIANCE CERTIFICATION

Research activities involving the use of human subjects, vertebrate animals, and/or biohazards must be reviewed and approved by the appropriate Texas A&M University regulatory research committee (i.e., IRB, IACUC, IBC) before the activity can commence. This requirement applies to activities conducted at Texas A&M and to activities conducted at non-Texas A&M facilities or institutions. In both cases, students are responsible for working with the relevant Texas A&M research compliance program to ensure and document that all Texas A&M compliance obligations are met before the study begins.

I, Chandler S. Lawson, certify that all research compliance requirements related to this Undergraduate Research Scholars thesis have been addressed with my Research Faculty Advisor prior to the collection of any data used in this final thesis submission.

This project did not require approval from the Texas A&M University Research Compliance & Biosafety office.

TABLE OF CONTENTS

Page

ABSTRACT

Application of MEMS-Based Inertial Gravimetry to the Planetary Sciences

Chandler S. Lawson
Department of Marine and Coastal Environmental Science
Texas A&M University

Research Faculty Advisor: Dr. Michael E. Evans
Department of Marine and Coastal Environmental Science
Texas A&M University

Gravimetry, the measurement of slight variations in gravitational acceleration, can be used to infer density distributions and structures in the crust of a planetary body. The vast majority of studies on bodies other than the Earth have been constrained to orbital surveys, restricting the resolution of the data. Conducting surveys on or near the surface would allow for higher resolution data to be collected and the ability to resolve the finer scale structure of planetary crusts. On Earth, such surveys are conducted using a device known as a gravimeter. Traditional gravimeters are relatively massive, expensive, and fragile which limits their suitability for planetary exploration.

In this thesis, a project that supports wider efforts to mature micro-electromechanical systems (MEMS) gravimeters is discussed. NASA has developed an instrument with the goal of using MEMS technology to conduct gravity surveys. The instrument, named HELIX, includes a MEMS inertial measurement unit (IMU) that contains an accelerometer triad – such as those found in most smartphones, though more sensitive. The use of a precision accelerometer triad for gravimetry is referred to as “inertial gravimetry.” The efforts that this project supports aim to

develop MEMS accelerometers that are sensitive and stable enough to qualify as gravimeters, which on Earth is the measurement of the solid Earth tides, and then utilize these devices for planetary exploration. Such devices are more robust and have lower mass, cost, and power requirements than traditional gravimeters making them well-suited for extraterrestrial applications.

ACKNOWLEDGEMENTS

Contributors

I would like to thank my faculty advisor, Dr. Michael Evans, for giving me the opportunity to intern and conduct research at Johnson Space Center and for his guidance and support throughout the entire experience. I would also like to thank Dr. Paul Niles for his guidance and support throughout this project as well. Thanks to the Astromaterials Research and Exploration Division at Johnson Space Center for being so accommodating for the past year and a half and to everyone at Jacobs Technology who facilitated a smooth transition into my position and then to teleworking during the COVID-19 pandemic.

Thanks also go to my friends, colleagues, and the department faculty and staff for making my time at Texas A&M University a great experience. Finally, thanks to my family for all of their encouragement, love, and support.

The HELIX instrument used for Application of MEMS-Based Inertial Gravimetry to the Planetary Sciences was provided by the Astromaterials Research and Exploration Science Division of Johnson Space Center.

All work conducted for the thesis was completed by the student independently.

Funding Sources

Undergraduate research was supported by an internship from Jacobs Technology, Inc.

This work was also made possible by the National Aeronautics and Space Administration. Its contents are solely the responsibility of the author and do not necessarily represent the official views of Jacobs Technology, Inc. nor the National Aeronautics and Space Administration.

1. INTRODUCTION

The gravitational field of a planetary body is directly proportional to the distribution of its mass. Based on this relationship, measuring changes in gravitational acceleration with changes in position and elevation can reveal density distributions in the subsurface. Thus, the measurement of the gravitational field is desirable in a variety of applications. For example, in natural resource exploration, the density distributions inferred from gravitational data can reveal dense mineral ore bodies, oil-containing sediments, and changes in natural gas saturation. In geodesy, gravity can be used to accurately define the shape of the Earth. In the Earth sciences, it has been used to map Earth's hydrological cycle, determine ocean bottom pressure, and help quantify sea level rise. Recently, the first gravity survey from the surface of Mars was conducted using one of the MEMS IMUs on the Curiosity rover (Lewis et. al., 2019). This survey highlighted the potential of using MEMS devices for geophysical and planetary exploration. Chapter 1 will give an overview of gravimetry, MEMS gravimeters, and inertial gravimetry.

1.1 Gravimetry

The development of modern gravimetry can arguably be traced back hundreds of years to the pendulum experiments of Galileo Galilei. Such pendulums began as timekeeping instruments and gradually developed into gravimeters due to the observation that the period of a pendulum is only dependent on its length and the local gravitational acceleration. Gravimeters have since developed into two broad categories: absolute and relative gravimeters. Absolute gravimeters perform absolute measurements of gravity by measuring the acceleration of a freefalling proof mass in a vacuum, whereas relative gravimeters determine gravitational acceleration relative to a baseline by measuring the displacement of a proof mass on a spring (Niebauer, 2015). The

following sections give an overview of gravity surveying and the platforms with which gravimetry is performed.

1.1.1 Gravity Surveying

There are a variety of factors that affect gravity readings during a survey. The first being variations in the gravity field due to planetary rotation and flattening. The centrifugal accelerations and forces experienced by rotating bodies cause slight deformations in their spherical shapes. As a planet rotates, the poles are flattened and the equator bulges outward. The resulting shapes were termed 'oblate spheroids' by Isaac Newton. This flattening causes the poles of a rotating body to be closer to its center of mass and thus have a higher gravitational acceleration, as evidenced by Newton's universal law of gravitation (Newton, 1687):

$$F = G\frac{m_1 m_2}{r^2} \tag{1.1}$$

where F is the force of gravitational attraction between two masses, $m_1$and m_2, where the centers of mass are separated by a radius of r. Conversely, the bulging causes a lower gravitational acceleration at the equator of the body. On Earth, the gravitational acceleration at sea level is 9.832186 m s^{-2} at the poles and 9.780327 m s^{-2} at the equator (Blakely, 1995). This is a difference of approximately 0.4% or 4 Gal. The unit 'Gal' is named for Galileo and is the common unit used in gravimetry. 1 Gal is equal to 1 cm s^{-2}.

One of the standard reference systems used for computing gravity at a point on the Earth's surface, known as the normal gravity, is the World Geodetic System 1984 (WGS84) reference ellipsoid. WGS84 is a close approximation to the gravitational equipotential surface and represents a rotating ellipsoid with its surface at mean sea level. The normal gravity can be computed using (Blakely, 1995):

$$g_{norm} = 9.783267714\left(\frac{1 + 0.00193185138639\,sin^2(\lambda)}{\sqrt{1 - 0.00669437999013\,sin^2(\lambda)}}\right) \tag{1.2}$$

where λ is latitude. The gravity vector on the surface of the ellipsoid has two components: gravitation and centrifugal acceleration as shown in figure 1.1.

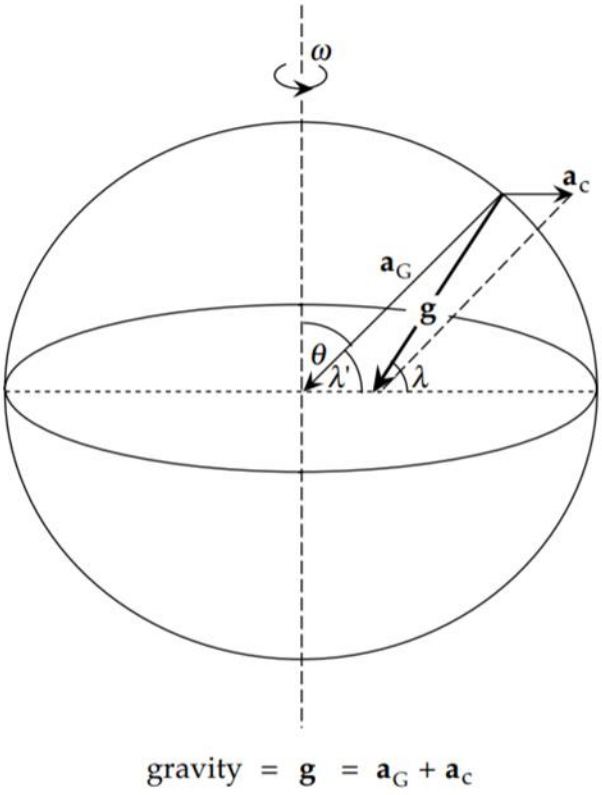

Figure 1.1 Gravity on the surface of the ellipsoid as a sum of gravitation and centrifugal acceleration. Reproduced from Lowrie, 2007.

Also derived from Newton's universal law of gravitation is the effect of elevation on Earth's gravitational field. By equating Newton's second law and the law of universal gravitation, Earth's gravitation can be computed:

$$g = G\frac{M_E}{r^2} \tag{1.3}$$

where M_E is the mass of the Earth. This relationship implies that the gravitational field attenuates as elevation increases above sea level, thereby increasing the radius from the Earth's

center of mass. Correcting for this effect results in the free-air gravity anomaly given by (Blakely, 1995):

$$\delta g_f = \frac{-2GM_E h}{R_E^3} \tag{1.4}$$

where h is the elevation above sea level and R_E is the radius of the Earth. Using the gravitational attraction and radius at sea level, the free-air anomaly is:

$$\delta g_f = 0.3086h \tag{1.5}$$

where there is a gravity gradient of -0.3086 mGal per meter of elevation gain. This effect is added to the observed gravity to correct the reading to what would be observed at sea level.

Elevation also affects the observed gravity through the gravitational attraction of mass between mean sea level and the elevation at which an observation is made. This mass causes an increase in the local gravitational acceleration and is assumed to be an infinite slab of rock with a uniform density. The resulting effect is known as the simple Bouguer anomaly given by (Blakely, 1995):

$$\delta g_b = 2\pi G\rho h \tag{1.6}$$

where ρ is the density of the slab of rock and h is the slab's thickness (elevation). This effect is subtracted from the observed gravity. Additionally, complex terrain such as hills or valleys can contribute to the observed gravitational acceleration. For example, if a measurement is taken near a hill, the hill's center of mass is at a higher elevation than the measurement point. This results in an upward gravitational acceleration, decreasing the observed gravity. If near a valley, the observed gravity would also decrease due to a lack of mass. To compensate for this effect, a terrain correction must be performed that essentially levels the terrain. To compute the terrain correction, a digital elevation model is typically used. The topography surrounding the

measurement location is divided into cylindrical vertical components and a correction for each component is computed depending on its elevation above or below the measurement point. The total correction is the sum of all individual corrections (Lowrie, 2007). This process is shown in figure 1.2.

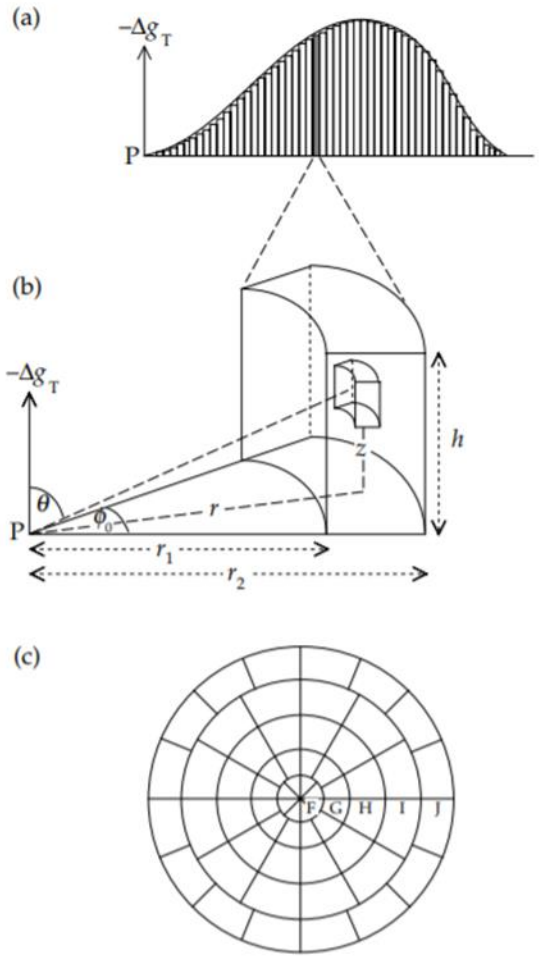

Figure 1.2. Terrain correction to observed gravity. (a) The topography is divided into vertical components, (b) corrections are computed for each component, (c) the sum of all individual components results in the total correction. Reproduced from Lowrie, 2007.

The sum of all aforementioned corrections to the observed gravity results in the complete Bouguer anomaly (Lowrie, 2007):

$$g_b = g_{obs} + \delta g_f - \delta g_b + \delta g_T - g_{norm} \tag{1.7}$$

where g_{obs} is the observed gravity and δg_T is the terrain correction. The effects considered in this study are represented by figure 1.3. There are additional factors to take into consideration when conducting gravity surveys such as the solid earth tides and ocean and atmospheric loading. These effects are on the μGal level and below the accelerometers' limit of detection, and as such, will not be discussed in this study.

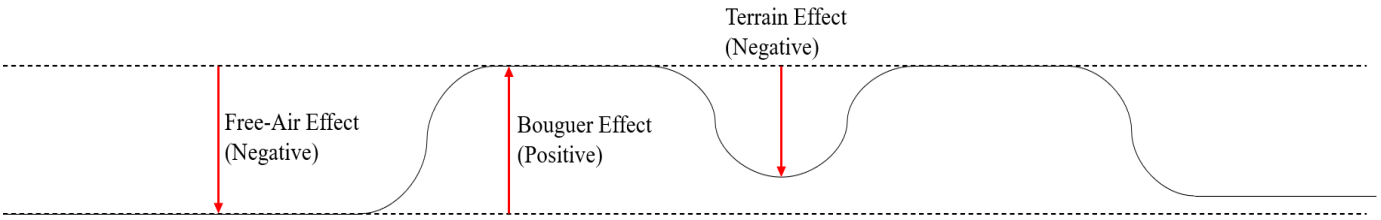

Figure 1.3. Effects of elevation, density, and topography on observed gravity.

1.1.2 Surface Gravimetry

Surface gravimetry concerns surveys conducted on the surface of the Earth or another body. The typical surface-based survey involves the gravimeter performing measurements in a static position at points along a traverse, though moving-base surveys may be conducted. Surface gravimetry allows for high resolution data to be collected since there is no limit on how closely spaced the survey points are. High accuracies are also achievable since the gravitational field strengthens with decreasing elevation. However, surface gravimetry is limited by the time-consuming nature of the surveys as well as large areas of the Earth's surface being inaccessible by land. This is true of other bodies as well, but since current data has almost exclusively been collected from orbit, higher resolution data collected from the surface would be invaluable for the exploration of such bodies.

1.1.3 Satellite Gravimetry

Launched in 2000, the CHAMP (Challenging Minisatellite Payload) satellite began spaceborne observations of Earth's gravity field (Reigber, Lühr, and Schwintzer, 2002). Two additional missions have since been launched into Earth-orbit: GOCE (Gravity Field and steady-state Ocean Circulation Explorer) and the twin GRACE (Gravity Recovery And Climate Experiment) satellites (Drinkwater et. al., 2003; Tapley et. al., 2004). In 2011, the GRAIL (Gravity Recovery And Interior Laboratory) satellite mission was launched with the goal of mapping the Lunar gravity field (Zuber et. al., 2013). On Mars, a global gravity model has been constructed as a composite of satellite tracking data, a reference gravity field, and modelling coupled with high-resolution laser altimetry data (Hirt et. al., 2012).

The GRACE and GRAIL missions consisted of satellite pairs which used satellite-to-satellite tracking to determine the mutual distances between each satellite. Variations in the mutual distances were due to local variations in gravitational accelerations. Thus, the variations in mutual distance allowed for gravity to be inferred. The GOCE mission used a gravity gradiometer that incorporated three accelerometer pairs to measure both gravity and gravity gradients.

While satellite gravimetry allows for the construction of global gravity models, the spatial resolution of the collected data is limited by both the platform's altitude of orbit and high inherent speed. The spatial resolutions achieved by each of the aforementioned missions are on the order of several to hundreds of kilometers. Thus, satellite gravimetry alone is insufficient for determining localized (tens of meters) gravity field variations at a sufficient resolution.

1.1.4 Airborne Gravimetry

Airborne gravimetry represents an efficient method of yielding gravity data with a higher resolution than satellite gravimetry. It can serve as an intermediate between satellite and surface gravimetry by covering the spatial scale gap between the two methods. Airborne gravity surveys are typically conducted by combining a gravimeter designed for airborne or seaborne applications with a global navigation satellite system (GNSS) receiver.

There are two ways in which a gravimeter is used in airborne operations and both are defined by the way the gravimeter is mounted to a vehicle, also known as the instrument's mechanization. These are the platform-stabilized mechanization and strapdown mechanization. The platform-stabilized mechanization keeps the gravimeter's measuring axis aligned with the vertical component of the gravity vector through the use of a mechanically stabilized platform. When in the strapdown mechanization, the gravimeter is fixed to the body of the vehicle. Strapdown gravimetry requires the use of an accelerometer triad since the vehicle body is not aligned with the vertical component of the gravity vector. The orientation of the accelerometer triad is determined by angular rate measurements taken from a triad of gyroscopes.

1.2 MEMS Gravimeters

In order to understand the significance of MEMS gravimeters, it is necessary to understand the significance of MEMS devices as a whole. MEMS devices encompass microscopic sensors fabricated using silicon. These devices can be mass produced with exceptionally low costs, sizes, and power requirements. Since the inception of such devices in the 1960s, the field has developed into many sub-fields, including inertial MEMS sensors – the sub-field under which MEMS accelerometers fall. In the 1990s, the precision of MEMS accelerometers increased from the mg level to the μg level (Wise, 2007). With 1 g being equal to

9.80665 m s^{-2}. While MEMS accelerometers have been used in a variety of applications, few have ever had the proper sensitivity and stability to qualify as a gravimeter.

In 2016, the first detection of the solid Earth tides with a MEMS device was performed, initiating the development of a new class of gravimeter (Middlemiss et. al., 2016). The device achieved a sensitivity of 40 μGal $Hz^{-1/2}$ – sensitive enough to measure the movement of magma beneath a volcano before an eruption – and is small enough to be mounted to a drone. Following this breakthrough, other highly precise devices have been developed (Tang et. al., 2019; Mustafazade et. al., 2020). Based on the design of Mustafazade et. al. (2020), an instrument is being developed that is dedicated to the exploration of extraterrestrial bodies (Lewis et. al., 2020). Additionally, the first mission concept that employs a MEMS gravimeter, GEMMA (Geophysical Exploration of the Moon with MEMS Accelerometers), has been proposed (Lewis et. al., 2019). These developments represent a paradigm shift for the geophysical exploration of the Solar System and the field of gravimetry as a whole.

1.3 Inertial Gravimetry

Inertial gravimetry is the use of a precision accelerometer triad rather than a dedicated gravimeter to conduct gravity surveys. The accelerometer triad is provided via an IMU that is designed for inertial navigation, not gravimetry. Inertial gravimetry has been utilized in geodetic applications for nearly three decades (Wei and Schwarz, 1998). The most common method has been to conduct airborne gravity surveys using a combined inertial navigation system (INS) and GNSS (Jekeli, 2012). One of the goals of an INS in navigation is to determine the kinematic accelerations of a vehicle for further processing, which requires the determination and removal of the gravitational acceleration from the INS acceleration measurements. Thus, it follows that this process could be reversed, and measurements of gravity could be made.

There are two types of inertial gravimetry: vector and scalar. Vector inertial gravimetry is the measurement of both the vertical and horizontal components of the gravity vector, whereas scalar inertial gravimetry only focuses on either the vertical component or the magnitude of gravity. This study is concerned with scalar gravimetry as a means for probing subsurface structure.

1.3.1 Accelerometers

MEMS-based inertial gravimetry provides a practical, low-cost method for the development of procedures, algorithms and modelling techniques that pertain to the development of MEMS gravimeters. However, there are a number of challenges that need to be addressed when performing inertial gravimetry. The first of these is that accelerometers measure the superposition of gravitational, g, and non-gravitational, x, accelerations known as the specific force f:

$$f = x - g \tag{1.8}$$

thus, the fundamental problem in inertial gravimetry is the separation of gravity from the total acceleration. In the moving scenario, this is typically accomplished through the differentiation of GNSS positions and some form of filtering. In the static case, non-gravitational accelerations could have various sources including seismic, anthropogenic, or environmental sources such as wind.

The second challenge is that accelerometers have inherent tilt-related bias and scale errors and, when in the tri-axial configuration, these errors occur along each accelerometer axis. Disregarding any external effects and noise, the output of the accelerometer triad can be modeled as (Titterton and Weston, 2004):

$$\begin{bmatrix} A_x \\ A_y \\ A_z \end{bmatrix} = \begin{bmatrix} a_x \\ a_y \\ a_z \end{bmatrix} \left(\begin{bmatrix} S_x & 0 & 0 \\ 0 & S_y & 0 \\ 0 & 0 & S_z \end{bmatrix} + I_{3\times3} \right) + \begin{bmatrix} b_x \\ b_y \\ b_z \end{bmatrix} \tag{1.9}$$

with raw measurements, A_i, true measurements, a_i, bias and scale errors, b_i and S_i, and the identity matrix, I. The bias error is the offset that can be observed when there are no external stimuli acting on the accelerometers. It can be interpreted as the force required to keep the proof mass in its zero position when there is no specific force applied to the accelerometer. The scale error, or scale factor, arises from errors in the analog-to-digital conversion of voltages to units of acceleration performed by the converter in the accelerometer. An error in the defined proportionality factor between the electric current and measured accelerations causes the output of the accelerometers to be scaled by a certain value. The bias and scale errors contain two components: a constant, deterministic component and a variable component that is usually temperature dependent (Titterton and Weston, 2004).

Additionally, accelerometers often exhibit time-dependent unidirectional drifts over long periods of operation, variations in the bias and scale errors between instrument power-ups, thermo-mechanical white noise, and vibration induced noise (Titterton and Weston, 2004). The accelerometers used in this study were contained within an IMU-3030 manufactured by MEMSense. The standard accelerometer characteristics are listed in Table 1.1 (MEMSense, 2019).

Table 1.1 IMU-3030 Accelerometer characteristics. [1]Typical to maximum values.

Axis	**Bias (µg)[1]**	**Scale Factor (ppm)[1]**	**Bias Temperature Coefficient (µg °C^{-1})**	**Scale Factor Temperature Coefficient (ppm °C^{-1})**	**Resolution (µg)**
x	±383 – 1959	±1205 – 2088	11.51 – 19.24	7.14 – 12.86	10
y	±383 – 1959	±1205 – 2088	11.51 – 19.24	7.14 – 12.86	10
z	±485 – 1982	±3243 – 4700	11.51 – 19.24	17.36 – 20.96	10

2. METHODS

In this chapter, the setting of a field test is introduced followed by the methods used to attempt static measurements of the Bouguer anomaly induced by lateral density variations in the subsurface.

2.1 Field Test

A field test of the instrument was carried out at the High Island salt dome on the Texas Gulf Coast. Three surveys were conducted along a traverse over the dome. Salt domes are diapiric structures that vertically migrate through the subsurface predominantly through differential loading of the overlying sediment (Jackson and Talbot, 1986). Salt has the ability to flow in the solid-state at relatively low temperatures and pressures thus, when the pressure caused by differential loading is high enough, the salt begins an upward intrusion into the overlying sediment.

The standard density of halite is 2.165 g cm^{-3}, typically lower than the sediments that surround most salt dome structures along the Gulf Coast (Anthony et. al., 2003; Talbot, 1993). The site was chosen because this should provide an apparent negative anomaly. In addition to density contrast, the site was chosen due to the dome being situated in the shallow subsurface with depths as shallow as approximately 120 meters (Halbouty, 1936). At these depths, the dome significantly uplifts the overlying surface, allowing the dome's boundaries to be approximated using a digital elevation model. The digital elevation model is shown in figure 2.1 and an elevation profile that encompasses the traverse is shown in figure 2.2.

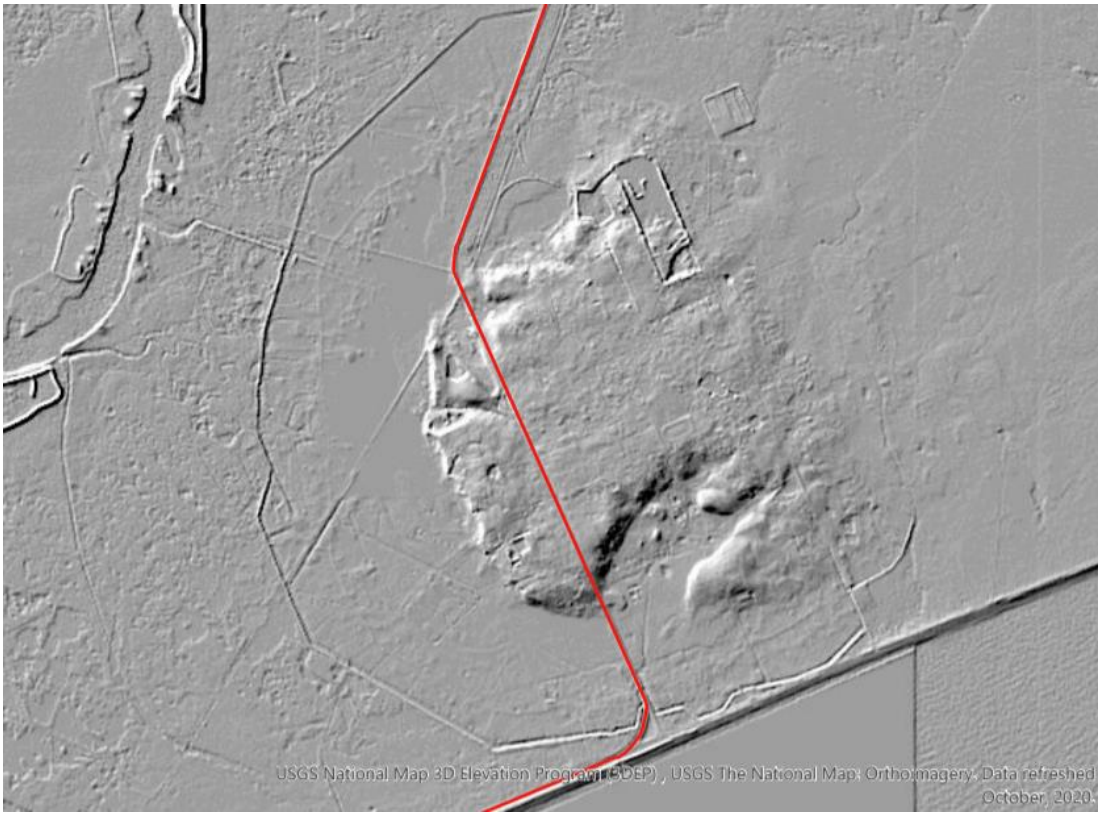

Figure 2.1. Digital elevation model of High Island overlain with traverse.

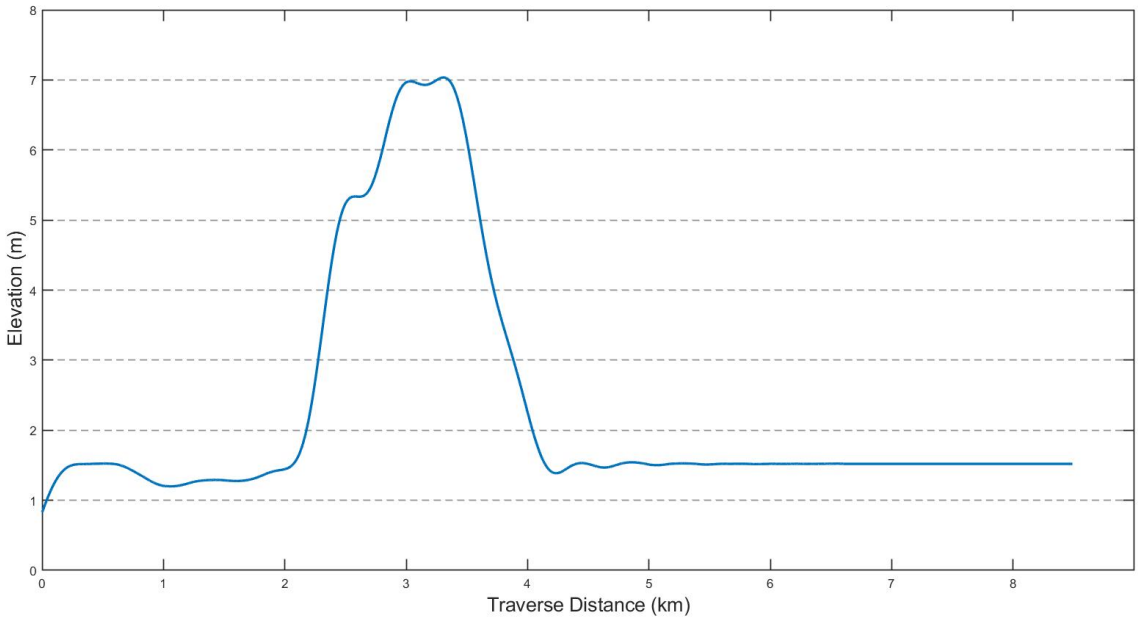

Figure 2.2. Elevation profile over the High Island dome.

A summary of the surveys is included in table 2.3. Initially, the points were planned to be spaced 100 meters apart. This proved to be unfeasible due to private property constraints, construction and highway barriers, and inundated areas were the traverse lies below sea level. Additionally, each survey contains a different number of points due to changes in construction over the three-week time period that the surveys were conducted. However, this is unproblematic because all points are crossover points between the surveys.

Table 2.1 Survey summary.

Survey Line	Date	Number of Data Points
1	03/14/2021	55
2	03/20/2021	78
3	03/27/2021	50

The accelerometers sample data at 800 Hz, which are decimated by a factor of 40 to produce 20 Hz samples. These data were then averaged to create 1-minute samples at each location. Environmental data were collected using a Dracal Technologies PTH-200. The environmental data were sampled at 1 Hz and averaged over the same interval as the accelerometer data.

2.2 Calibration and Noise Compensation

2.2.1 Non-Linear Regression

As previously stated, accelerometers typically exhibit long-term unidirectional drift and temperature-dependent bias drifts. The thermal drifts can arise from the behavior of the internal electronics in response to temperature instabilities and from the thermal expansion of silicon (Titterton and Weston, 2004; Watanabe, Yamada and Okaji, 2004; Middlemiss et. al., 2016).

Laboratory calibration methods exist that aim to reduce thermal drifts; an overview can be found in Becker (2016). These methods generally require equipment such as precision rate tables and thermal chambers. In the absence of such equipment, a simpler method must be performed.

Various regression techniques have been used to model drifts that are temperature or time-dependent (Becker et. al., 2015; Middlemiss et. al., 2016; Lewis et. al., 2019). In this study, non-linear least squares regression is chosen to model the response of the accelerometers to external effects. Non-linear least squares regression is used to fit a set of observations to a set of unknown parameters using a model that is non-linear. The non-linear model is successively approximated using a linear model and the parameter estimates are continuously tuned until a suitable fit is established (Seber and Wild, 2005).

The model developed for this study accounts for survey duration d, and variations in sensor temperature T_{imu}, ambient temperature T_{amb}, and barometric pressure, p. The bias and scale errors are modeled as constant offsets in the data given that the IMU remains powered over the duration of each survey and that relative changes in gravity are of concern. Instrument drifts are considered more important in the relevant literature, where residual constant offsets are corrected using least-squares adjustments based on crossover points or gravity models (Glennie and Schwarz, 1999; Hwang et. al., 2006; Ayres-Sampaio et. al., 2015). Additionally, the gravity corrections from equation (1.7) are used to estimate the simple Bouguer anomaly. The terrain correction was neglected due to the flatness of the terrain around the dome. The correction is applied to the difference between the raw accelerometer data and the gravity corrections such that the Bouguer anomaly estimate will lie within the model residuals, ϵ:

$$g_B = \sqrt{A^T A} + (\beta_1 d + \beta_2 T_{imu} + \beta_3 T_{amb} + \beta_4 p) + \delta g_f - \delta g_b - g_{norm} + \epsilon \tag{2.1}$$

where A is equivalent to equation (1.9), and β_n denotes the coefficients that represent the effect of the parameters on the accelerometer outputs. Note that the inclusion of barometric pressure variations in the model is novel. Multiple laboratory datasets indicate a correlation between the output of the accelerometers and variations in barometric pressure, though the reason for this is unclear.

2.2.2 Wavelet Denoising

As will be shown in the next chapter, the residuals of the model will still be corrupted by noise. There could be a number of sources for this remaining noise such as random vibrations caused by wind or passing vehicles given that the traverse lies along a state highway. Here, wavelet shrinkage denoising is used to mitigate these effects. Wavelets are mathematical functions that can be used to partition signals into different scales based on frequency components and localize various features in the signal (Donoho and Johnstone, 1994). This allows features of interest to be retained whilst reducing noise. An additional benefit is that while traditional smoothing techniques generally remove only the high frequency noise components, wavelet denoising attempts to remove all noise components. The method has been successfully applied to inertial navigation and gravity data collected via inertial gravimetry (Nassar and El-Sheimy, 2005; Bruton et. al., 2000; Li and Jekeli, 2004; Li and Jekeli, 2008). The principle used in this study is that the underlying gravity signal should be correlated among the different surveys, and the random noise should be uncorrelated. By partitioning the signals into different components, comparisons of each component can be made.

An in-depth description of wavelet shrinkage denoising can be found in Donoho and Johnstone (1994) and Donoho (1995). Here, a general overview is provided. Assuming that $y\ t$ is a function representing the gravity data, the function can be decomposed into two parts:

$$y(t) = g(t_i) + \sigma\varepsilon_i, \qquad i = 1, \dots, n \tag{2.2}$$

where $g(t_i)$ is the underlying gravity signal and $\sigma\varepsilon_i$ represents the additive noise. The decomposition is performed using wavelet coefficients. First, the wavelet coefficients Y are obtained by applying the discrete wavelet transform W to the signal where a convolution is performed using scaling coefficients:

$$Y = W\{y(t)\} \tag{2.3}$$

The wavelet transformation of a signal in the time-domain is essentially the projection of the signal onto a set of functions that are the result of compressing and scaling a single function known as the mother wavelet. Examples of mother wavelets are shown in figure 2.3.

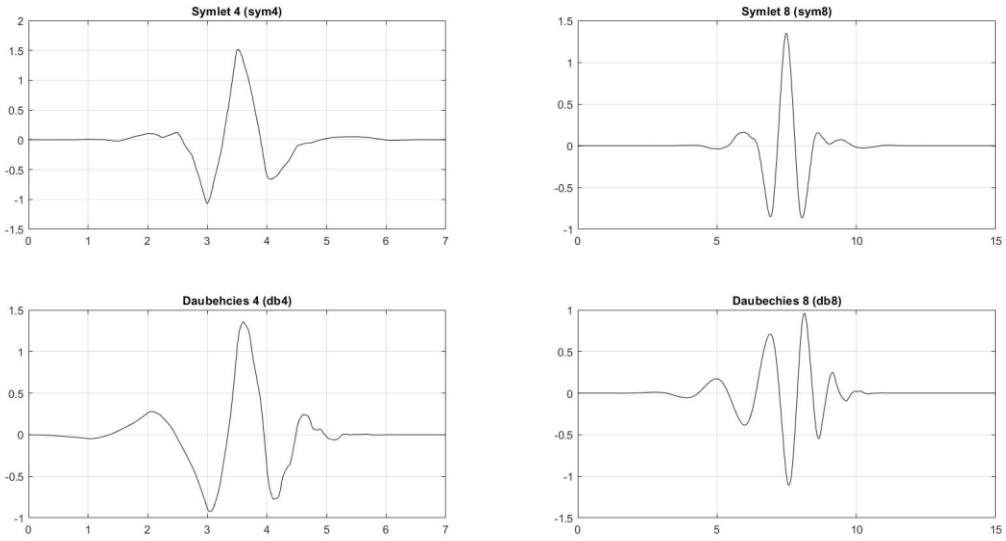

Figure 2.3. Examples of mother wavelets from the Symlet and Daubechies families of wavelets.

The coefficients are processed through a method called thresholding. The underlying signal is associated with only a few large coefficients, thus by removing (shrinking) the smaller coefficients associated with noise, the underlying signal can be reconstructed with much of the

noise removed. There are two thresholding methods: hard and soft. Here, a soft threshold is used, details on thresholding can be found in Donoho (1995):

$$D^s(d|\lambda) = \begin{cases} 0, & for\ |d| \leq \lambda \\ d - \lambda, & for\ d > \lambda \\ d + \lambda, & for\ d < -\lambda \end{cases} \tag{2.4}$$

where d denotes the wavelet coefficients and λ is the threshold value. Following thresholding, the inverse wavelet transform is used to reconstruct the denoised signal:

$$\hat{g}(t_i) = W^{-1}\{Z\} \tag{2.5}$$

where $g(t_i)$ is the denoised signal and Z denotes the processed wavelet coefficients.

3. RESULTS

In this chapter, results from laboratory analyses are presented followed by the initial results of the field tests.

3.1 Laboratory Analyses

The calibration model used in the field tests was developed based on laboratory analyses of static data. It was found that the accelerometers have a warm-up period of approximately 25-minutes. To be certain that this effect did not show up in the field data, the instrument was allowed to warm-up for 30-minutes before each survey. The warm-up effect in laboratory data is shown in figure 3.1.

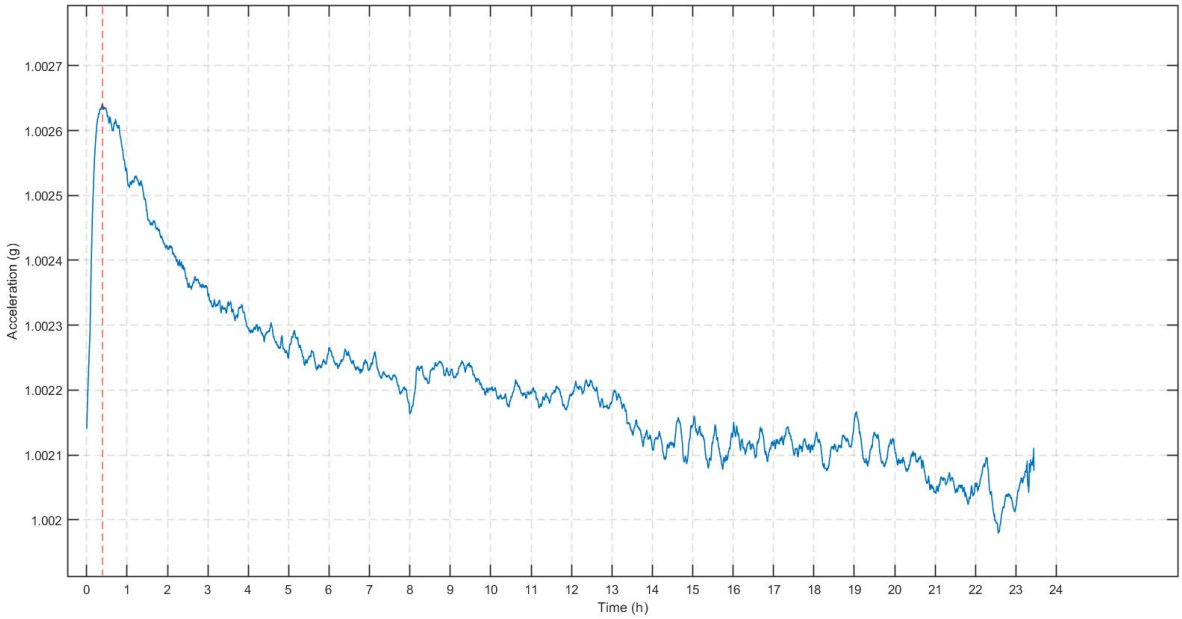

Figure 3.1. Instrument warm-up effect. The duration of the effect is denoted by the red line.

The effects of variations in sensor temperature, ambient temperature, and barometric pressure are shown to be repeatable across multiple datasets where significant variations occur.

A long-term unidirectional drift is observed across all datasets. The correlations between each individual parameter and measured accelerations are shown in figures 3.2 to 3.4, the linear drift is shown in figure 3.5, and a combined model with only linear terms is shown in figure 3.6. The specific dataset shown was collected over a period of 12-hours.

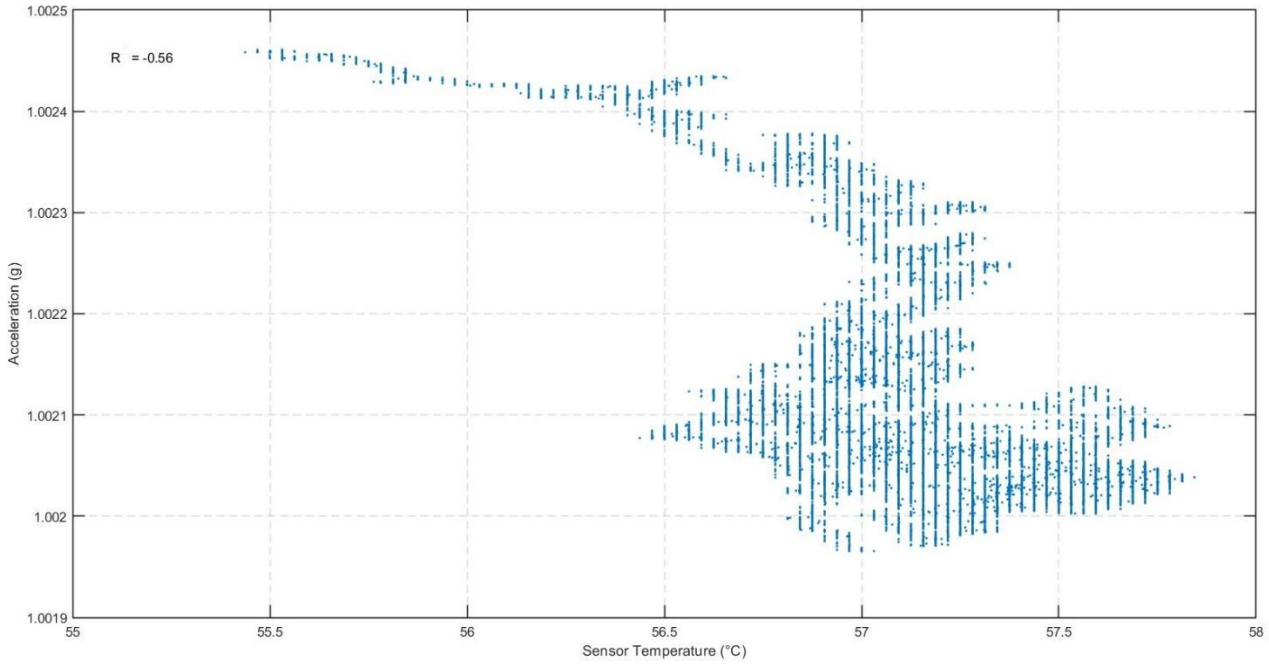

Figure 3.2. Total acceleration readings from the three accelerometers versus sensor temperature.

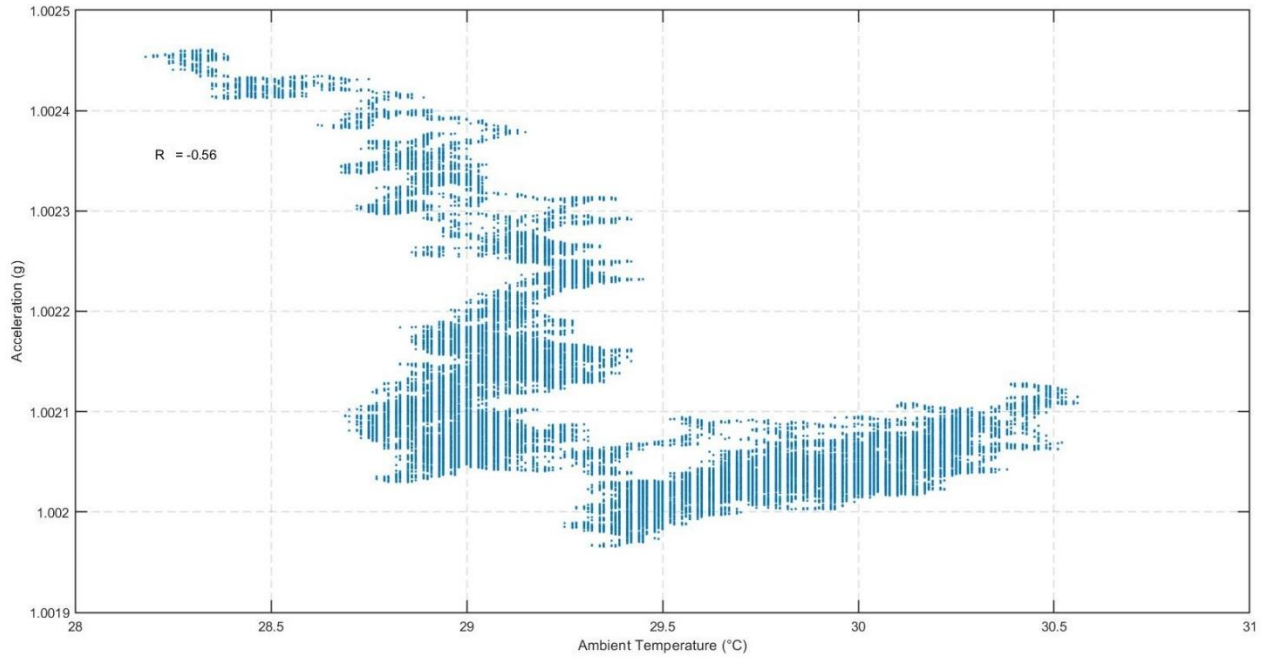

Figure 3.3. Total acceleration versus ambient air temperature.

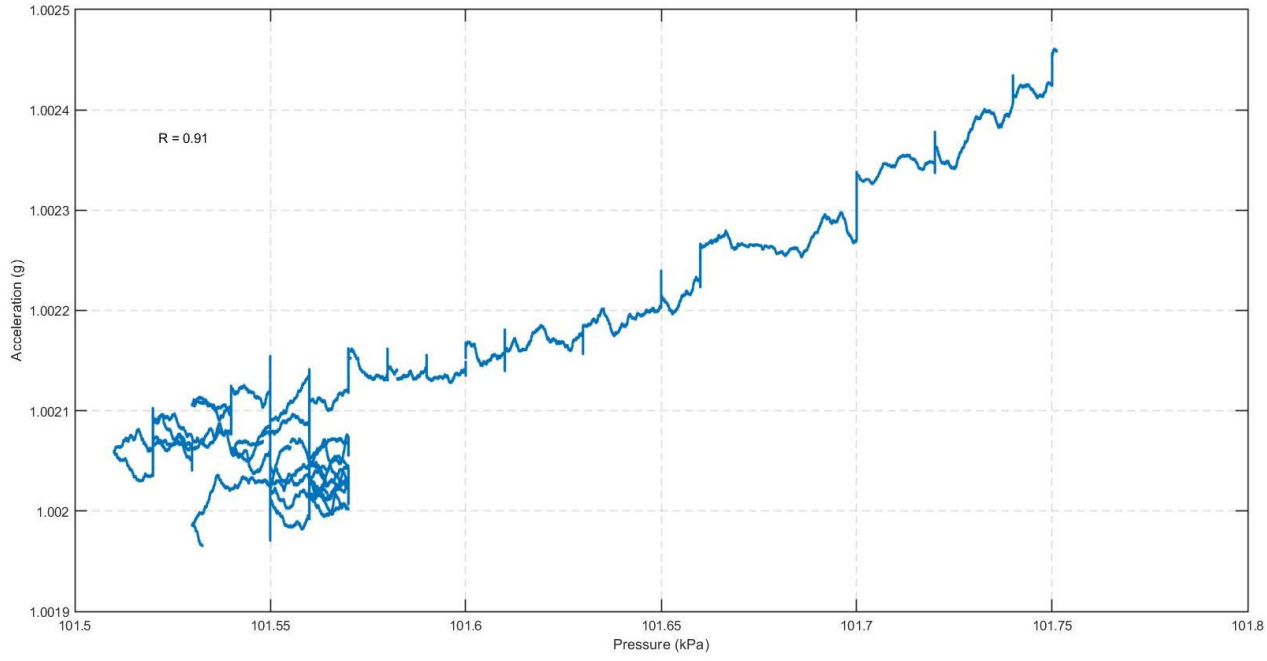

Figure 3.4. Total acceleration versus barometric pressure.

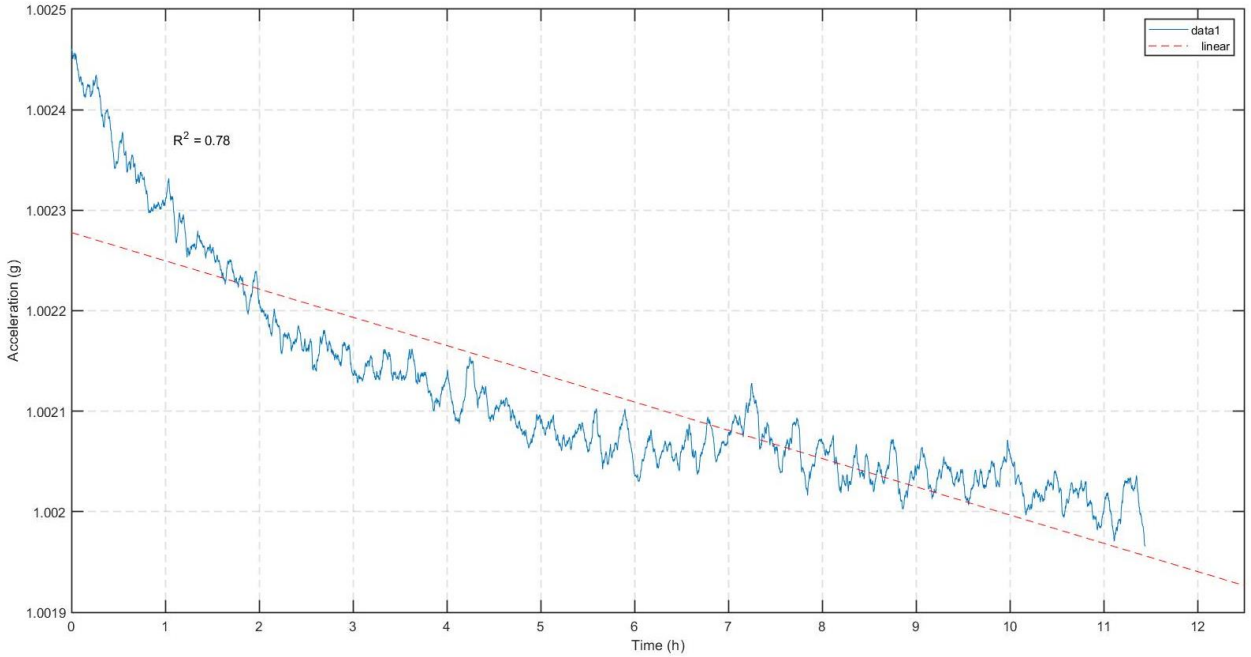

Figure 3.5. Observed linear drift over 12-hours.

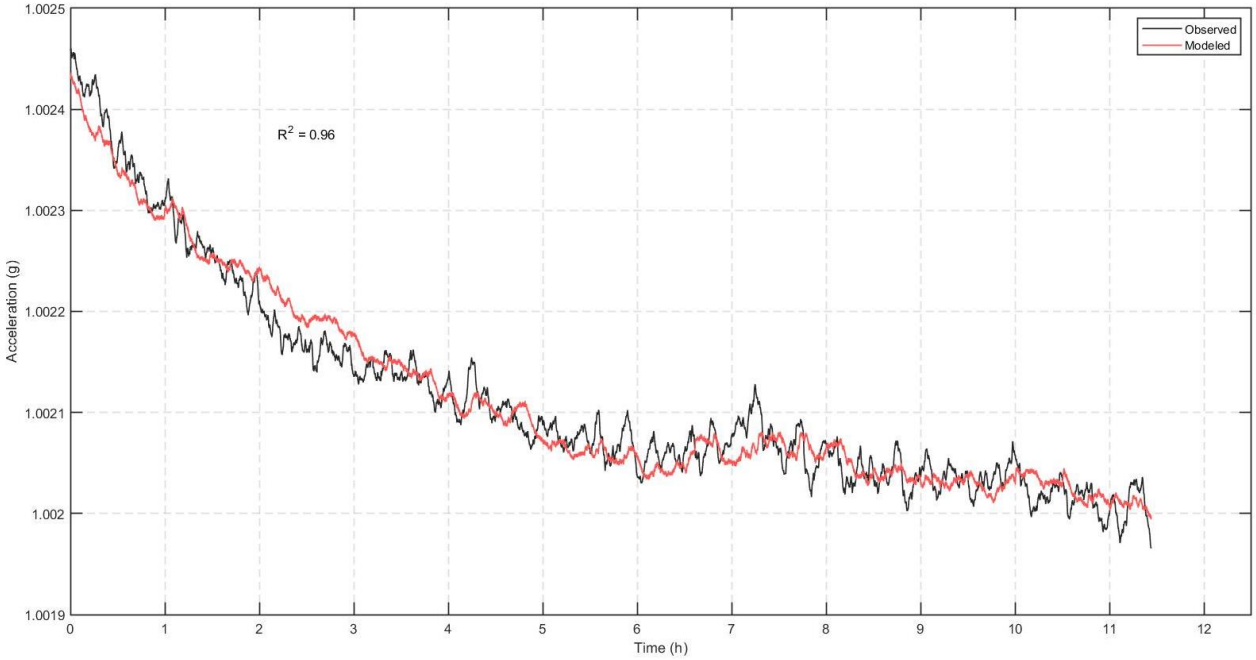

Figure 3.6. Combined drift model of the accelerometer triad. The residuals of the model are 20 mgal. Residuals can be reduced to 15 mgal with a quadratic term for pressure. All terms are statistically significant.

The bias and scale errors were estimated using a linear estimation algorithm (Lötters et. al., 1998). It was found that while the estimation error was low, significant offsets relative to the proposed application were still present. This contributed to the decision to include the errors as constant offsets in the model.

3.2 Field Test Results

After fitting the data from the three surveys with the above parameters and constant offsets, it was found that for all three surveys the scale factor terms were statistically insignificant. Upon further investigation, it was determined that the scale errors were absorbed by the bias estimates. This is consistent with the fact that when the instrument is static during a continuous survey, the scale errors can become indistinguishable from the biases (Farrell et. al., 2019). Therefore, all scale terms were eliminated in the models.

It was theorized that dynamic pressures induced by wind may introduce additional noise to the datasets. Therefore, terms to account for the effect of wind were added to the models. Wind speed, gust, and direction data were obtained from a NOAA weather station at High Island (NOAA, 2021). The station collects data at 6-minute intervals. The data were linearly interpolated to the start and end point of each 1-minute averaging interval for the accelerometer data and then averaged. Only wind speed was found to have a significant effect on the data. Wind gusts could have a significant effect; however, given the transient nature of wind gusts and the relatively long interpolation period of 6-minutes, it is likely that the interpolation is unable to yield accurate values for wind gusts. A summary of the results of the initial models are shown in table 3.1. Figures 3.7 to 3.9 show the results of each model with means removed from the raw and fitted data for clarity.

Table 3.1. Survey calibration model summaries.

Survey	Residuals (mgal)	Variance Reduction (%)
1	35	88
2	29	98
3	30	87

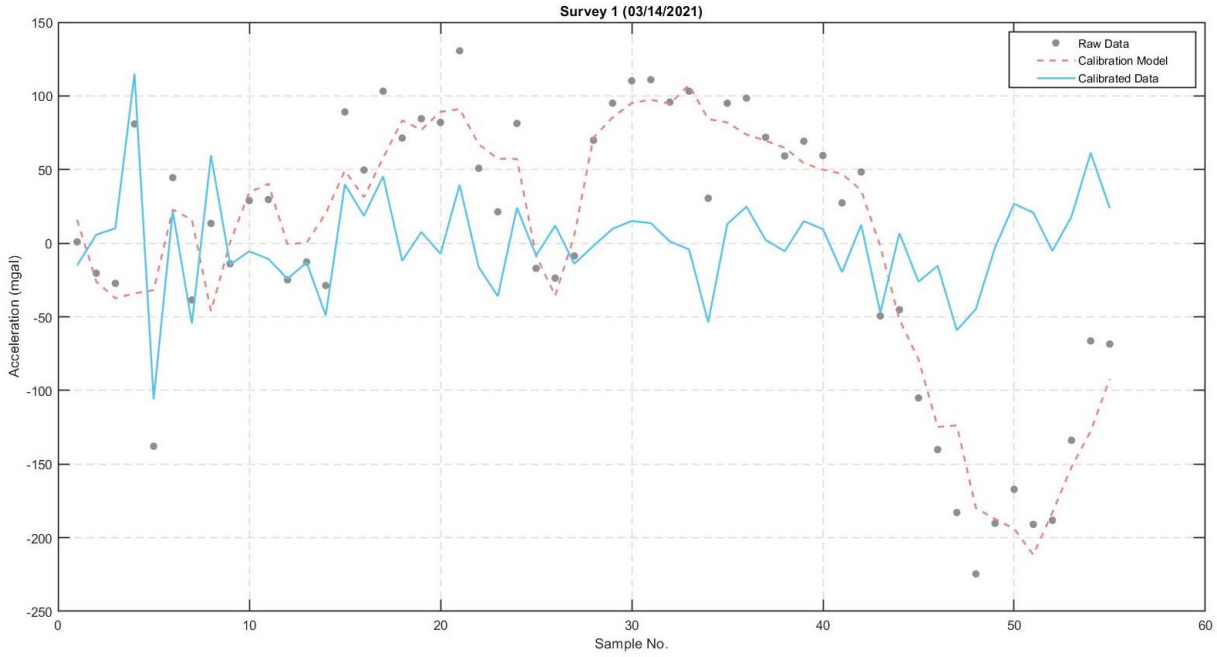

Figure 3.7. Survey 1 calibration results. The source of the large amount of variance at the start of the survey is unknown, though it could be due to a prolonged instrument warm-up.

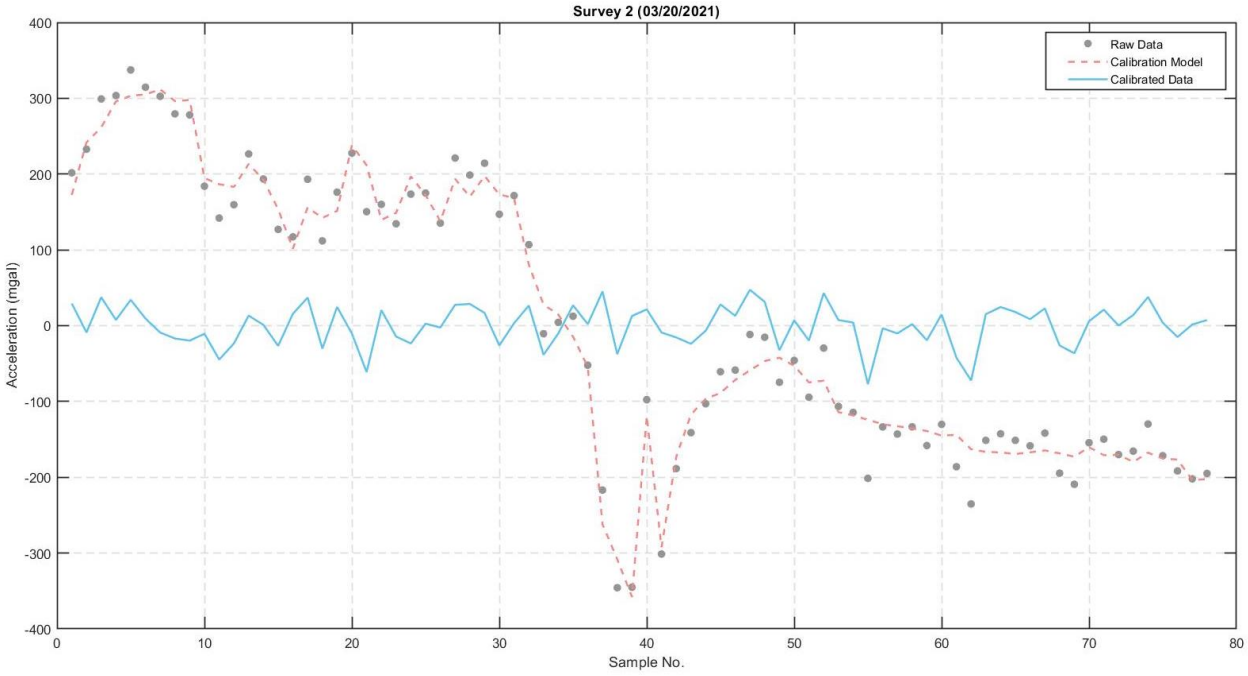

Figure 3.8. Survey 2 calibration results.

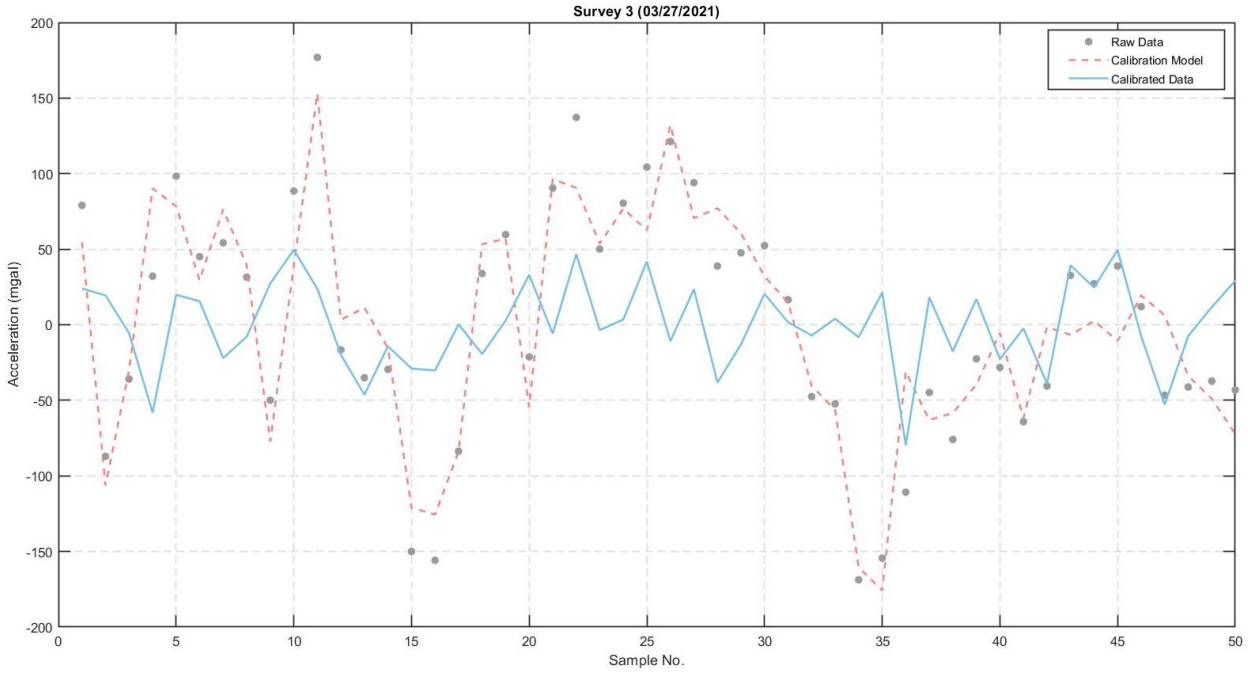

Figure 3.9. Survey 3 calibration results.

The correlation matrices of the models were obtained by computing the covariance matrix for each model. It was found that a high degree of multicollinearity among the environmental parameters is present. Namely, between survey duration and barometric pressure, and between the two temperature terms. The correlation matrices are shown in figures 3.10 to 3.12. w denotes the term for wind speed.

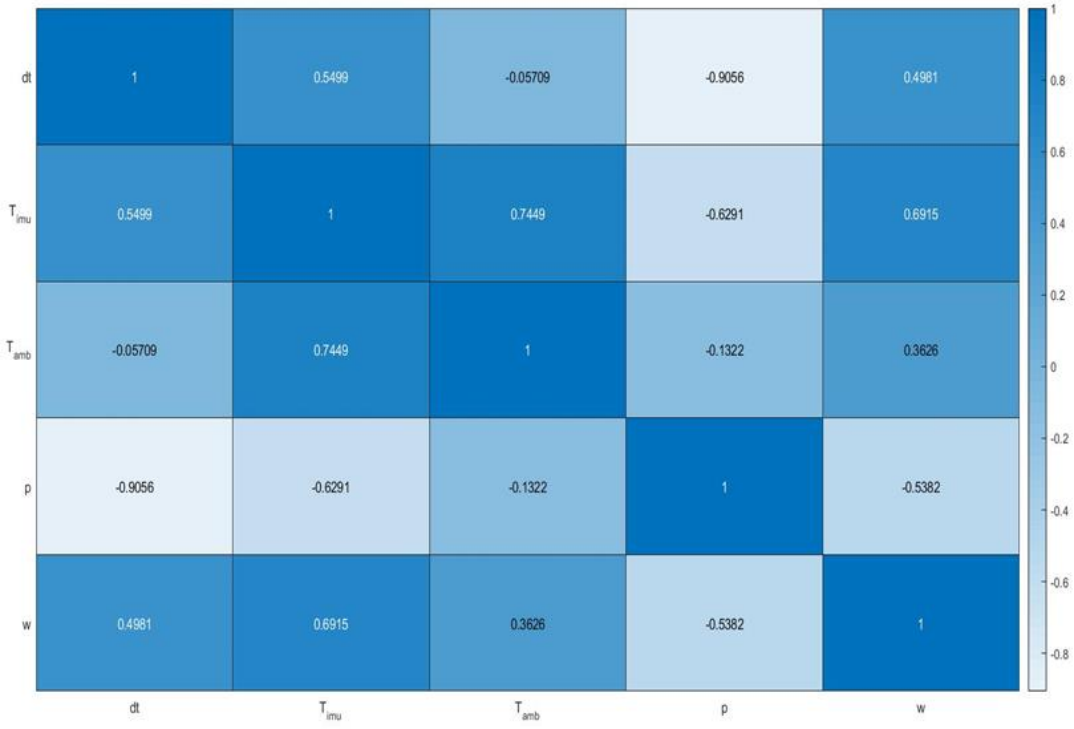

Figure 3.10. Survey 1 model correlation matrix.

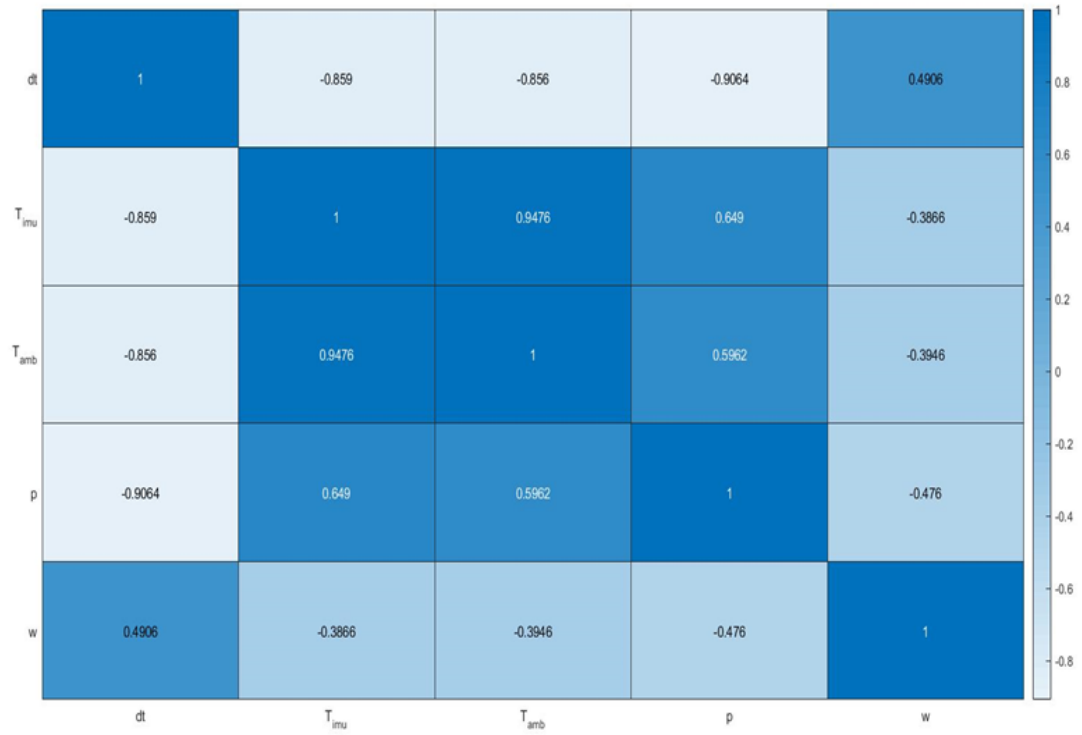

Figure 3.11. Survey 2 model correlation matrix.

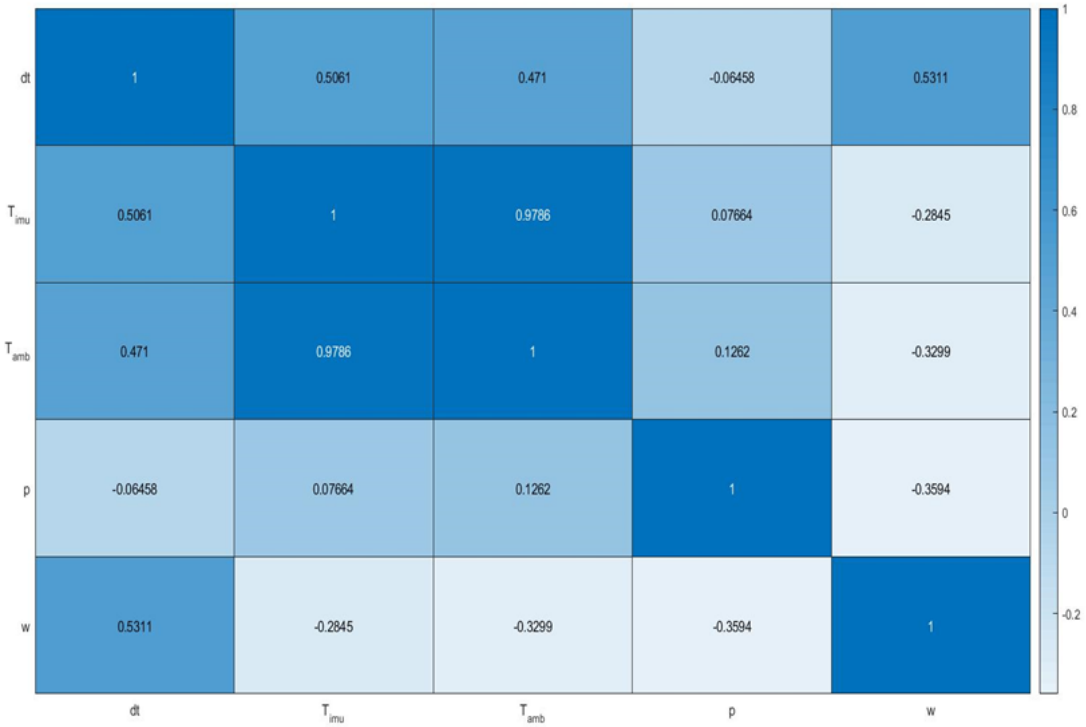

Figure 3.12. Survey 3 model correlation matrix.

This collinearity causes redundant information to be contained within the predictor variables and reduces the stability of the models. However, as the laboratory data shows, the parameters are all significant contributors to accelerometer drifts even when uncorrelated. In the field test data, the collinearity between the temperatures is likely due to the ambient temperature being the primary driver of variations in sensor temperature as opposed to mechanical and electrical self-heating of the IMU in the lab. Additionally, ambient temperature affecting the data acquisition module that is connected to an instrument control laptop could be an additional source of noise, along with affecting other electronic components not contained within the IMU enclosure. Therefore, in order to remove the multicollinearity while retaining non-redundant variance due to parameters that would otherwise be removed from the model, principal component analysis (PCA) is used.

PCA is used to find direction vectors of best fit lines through the data such that each vector is orthogonal to the previous vectors, known as the principal components (PCs). The PCs are the eigenvectors of the predictor variables' covariance matrix and are constructed as linear combinations of the predictor variables (Jolliffe, 1986). The number of PCs is equal to the number of predictor variables with most of the information in the original variables being contained in the first few PCs. The resulting variables are uncorrelated and contain the maximum amount of information from the original variables with redundant information removed. In the models, the drift terms are replaced by their PCs. The resulting correlation matrices are shown in figures 3.13 to 3.15. Even though the models using PCA are almost identical to the original models, they are still shown in figures 3.16 to 3.18 for completeness. A summary of the models using PCA is shown in table 3.2.

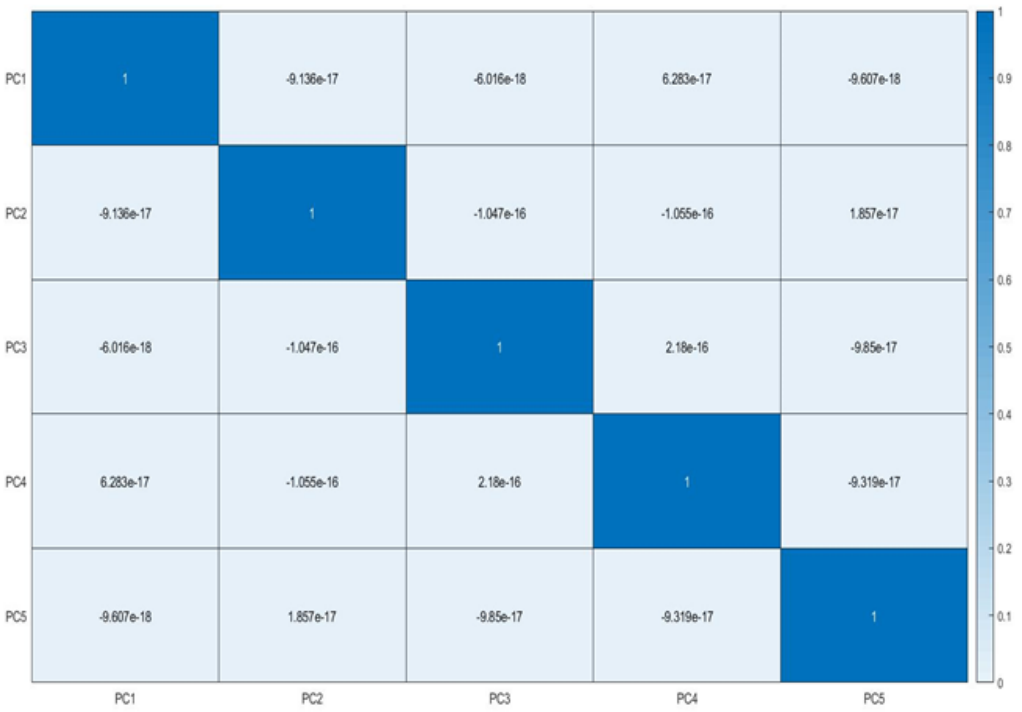

Figure 3.13. Survey 1 model correlation matrix using principal components.

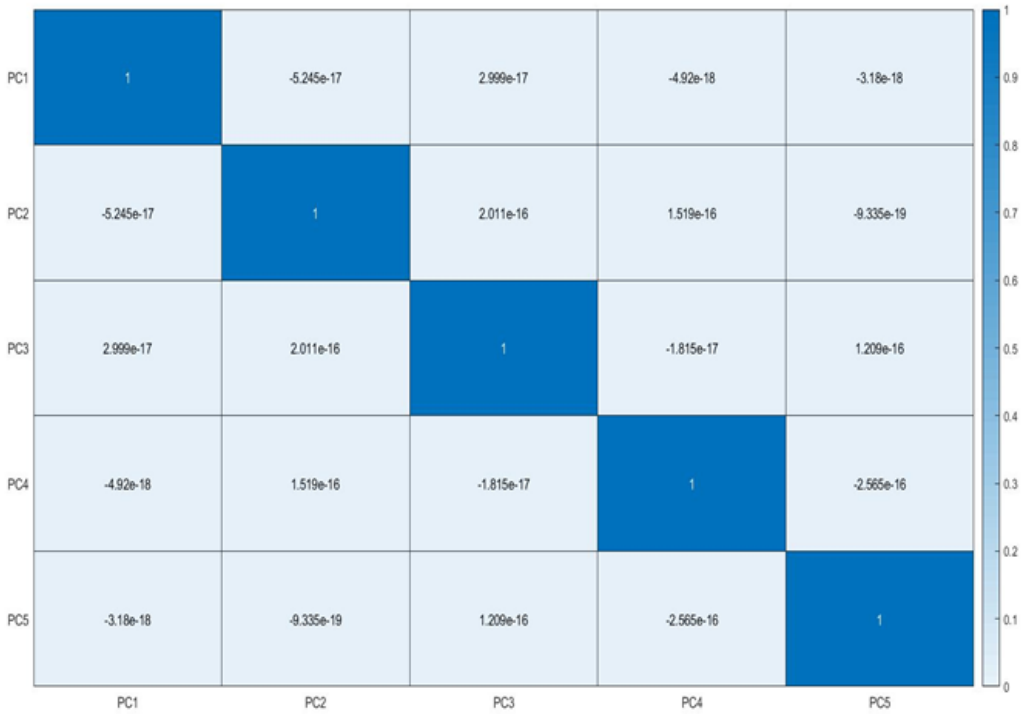

Figure 3.14. Survey 2 model correlation matrix using principal components.

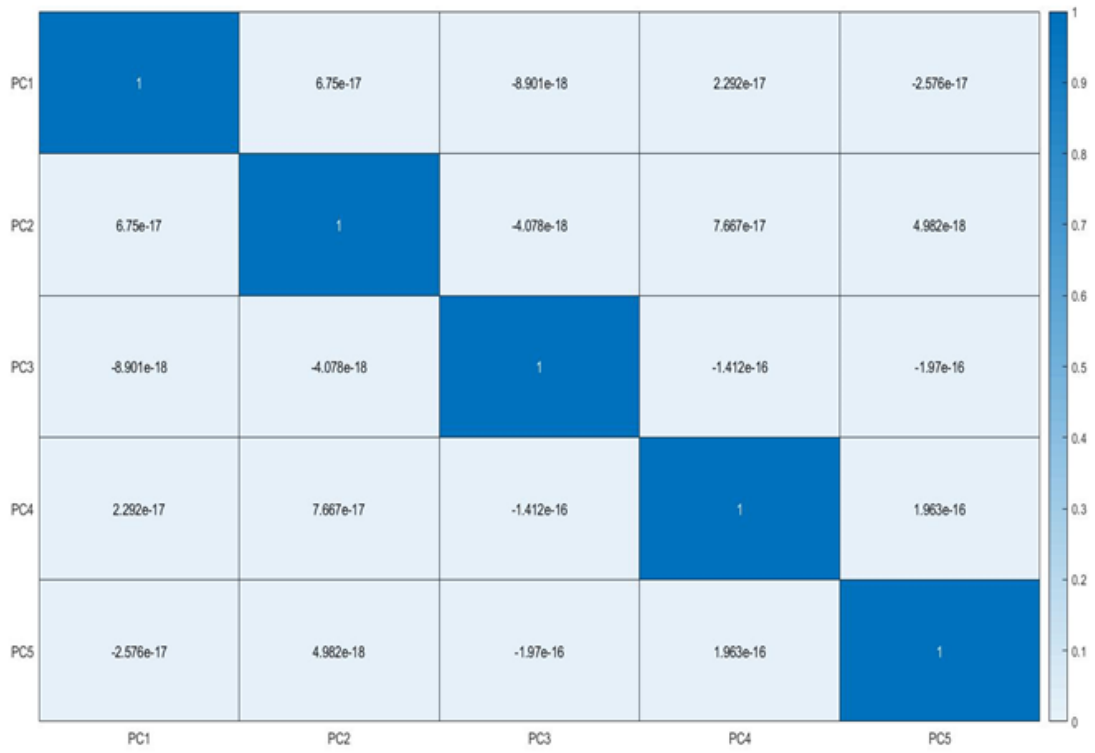

Figure 3.15. Survey 3 model correlation matrix using principal components.

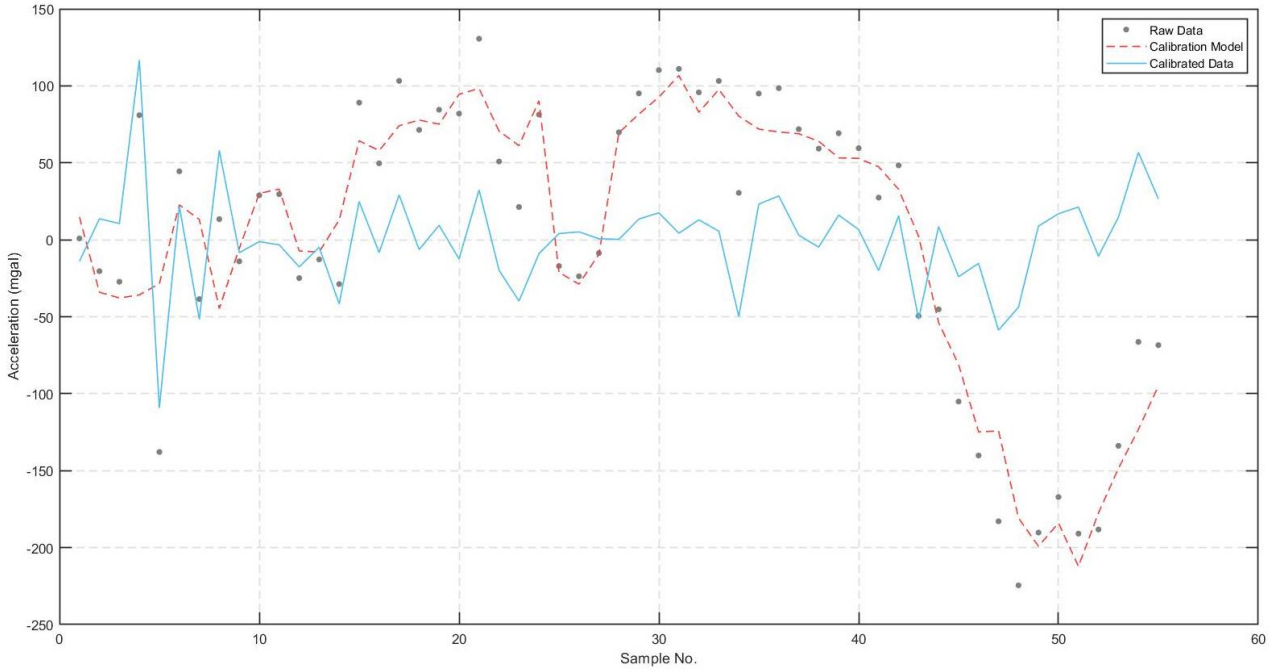

Figure 3.16. Survey 1 model using PCA.

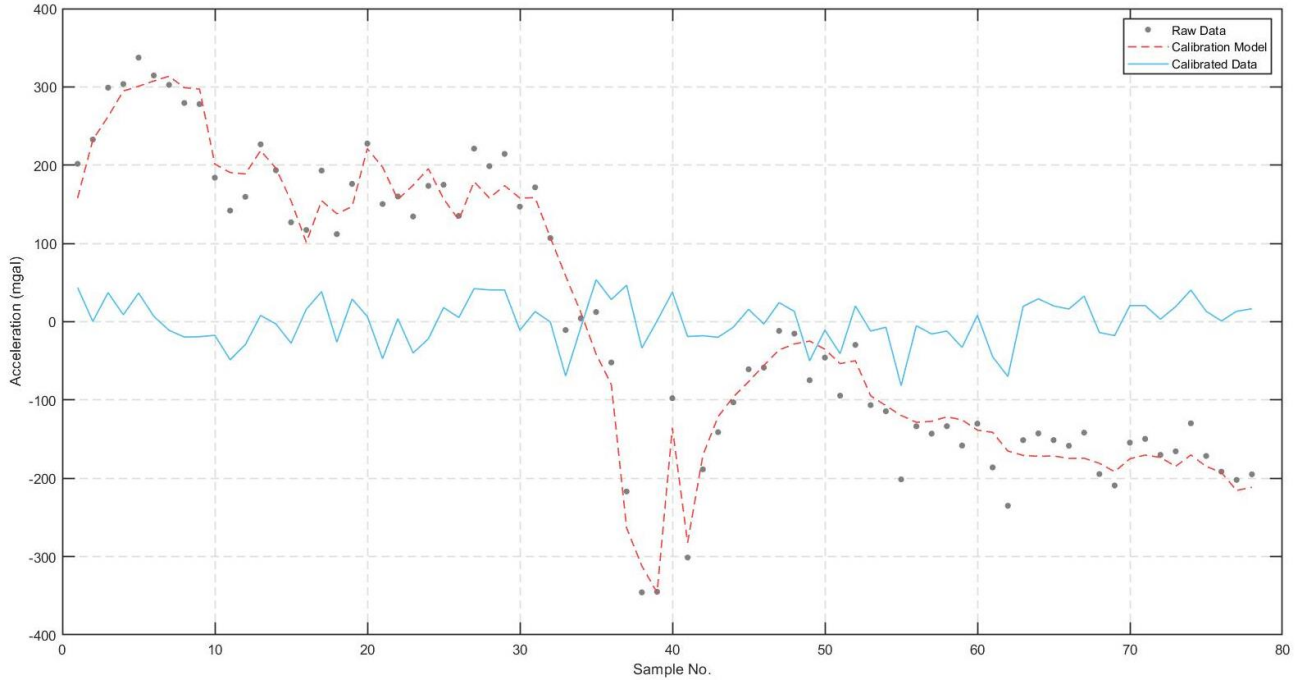

Figure 3.17. Survey 2 model using PCA.

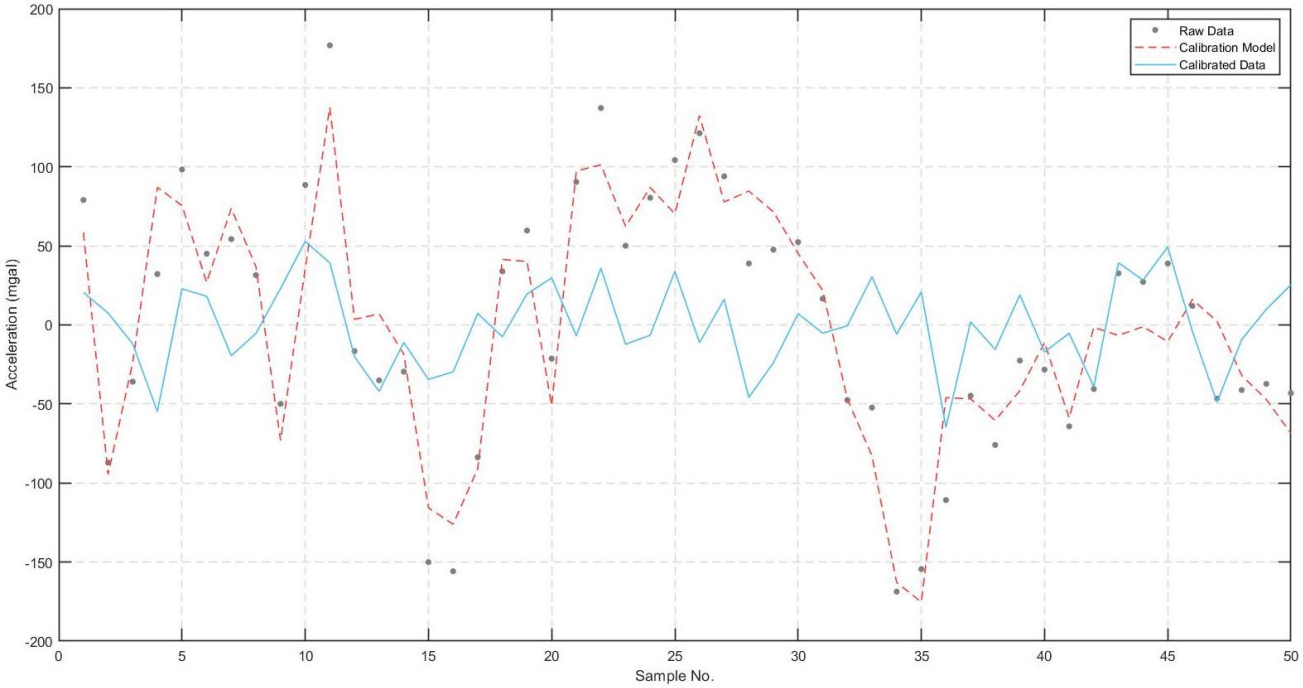

Figure 3.18. Survey 3 model using PCA.

Table 3.2. Summary of models using PCA.

Survey	Residuals (mgal)	Variance Reduction (%)
1	33	88
2	29	97
3	28	88

The residuals are relatively large when compared to results from the laboratory analyses and the specified resolution of the accelerometers. There could be a variety of sources for this residual noise such as the uncompensated wind gusts and passing vehicles on the nearby highway. The residuals were decomposed into 5 levels using the discrete wavelet transform. The corresponding levels for each survey were compared against one another where a large threshold value was applied to levels containing uncorrelated signals and smaller coefficients. The decompositions are shown side-by-side for a visual comparison in figure 3.10.

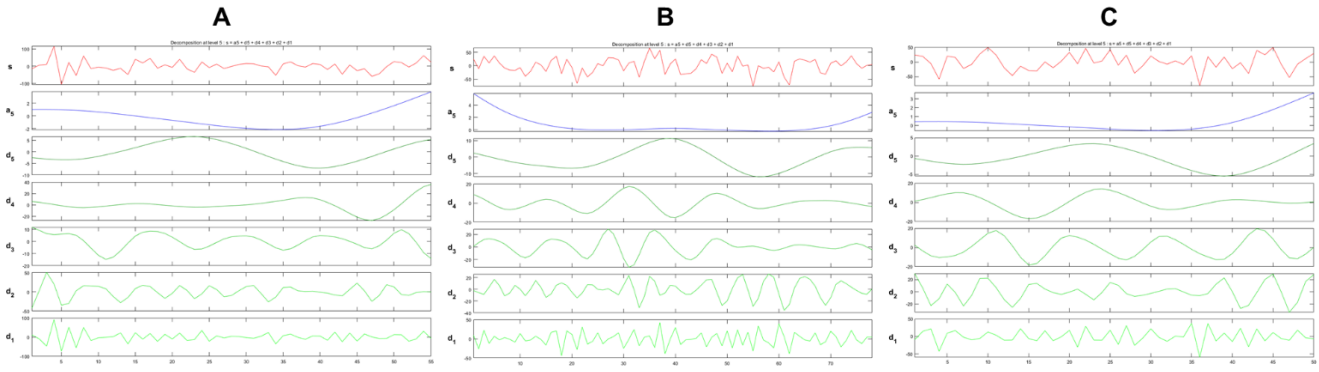

Figure 3.10. Wavelet decompositions of model residuals. A) Survey 1. B) Survey 2. C) Survey 3. The highest correlations occur in the approximation level (a_5) and detail level 5 (d_5).

The highest correlations occur in levels a_5 and d_5. The uncorrelated levels are given larger threshold values and all of the coefficients in the correlated levels are retained. The signals were then reconstructed. The final estimates all have precisions of approximately 10 mgal. Table 3.3 shows the correlations between the three surveys through 50 crossover points (all points of survey 3). Figure 3.11 shows the final anomaly estimates through the same 50 points.

Table 3.3. Correlation coefficients of the surveys.

Surveys	**R**
1,2	0.15
2,3	0.89
1,3	0.26

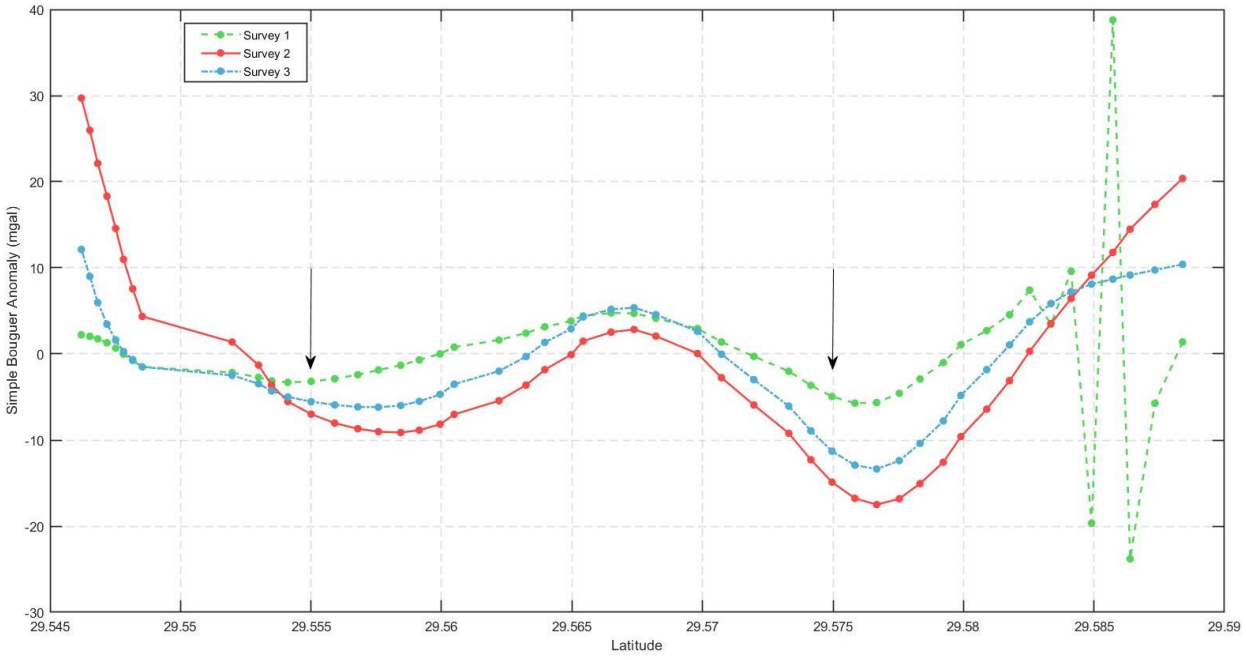

Figure 3.11. Bouguer anomaly estimates over the High Island salt dome. The black arrows denote the boundaries of the dome approximated using the digital elevation model.

The low correlation of survey 1 is due to the large variance at the northern endpoint of the survey. When these points are removed, the correlations increase to 0.55 and 0.85 for surveys 2 and 3, respectively. The source of this variance is unknown, though it may be due to a more prolonged instrument warm-up time.

4. DISCUSSION, FUTURE WORK & CONCLUSION

4.1 Discussion

The positive Bouguer anomaly estimate over the salt dome was initially unexpected. While most sediments are deposited with densities lower than that of salt domes, they compact, dehydrate, or lithify to greater densities than when deposited (Jackson and Talbot, 1986). The densities of sediments along the Northwestern Gulf Coast range from 2.51 – 2.95 g cm^{-3}, which should provide a positive density contrast with rock salt (Murray, 1961; Baker, 1995).

In the 1930s, core samples were taken at the High Island dome. It was found that a series of cap rocks existed above the dome (Halbouty, 1936). The top layer of the caps is composed of compact sand and limestone (ρ = 1.55 – 2.75 g cm^{-3}) with caps at increasing depths composed of calcite (ρ = 2.71 g cm^{-3}), gypsum (ρ = 2.31 g cm^{-3}), and massive anhydrite (ρ = 2.95 g cm^{-3}), with the anhydrite permeating through the lower layers (Halbouty, 1936; Anthony et. al., 2003). The uniform anhydrite cap that lies just above the salt is the dominant member of the series. Given the high density of anhydrite relative to the Quaternary sediments surrounding the dome (ρ = 2.51 g cm^{-3}), it is feasible that the cap rock could induce a positive anomaly (Murray, 1961).

It is not unheard of for dense salt dome cap rocks to induce a positive gravity anomaly signature (Jenkins, Messfin, and Moon, 1983). Gravity gradiometry data acquired at the Vinton salt dome in Louisiana shows the cap rock inducing a strong positive anomaly signal on all components of the gradient (Ennen and Hall, 2011). A gravity survey from a dome in Denmark showed a positive Bouguer anomaly caused by a thick cap rock within a wider low anomaly caused by salt, though the magnitude of the anomaly is smaller than observed for the High Island dome (Ramberg and Lind, 1968). Benassi et. al. (2006) in particular found that even in the

absence of a dense caprock, a salt dome can still produce a positive anomaly when the dome pierces all sedimentary layers.

The results of the field test align well with previous studies of domes in the shallow subsurface and domes which have high density cap rocks. The results are promising when compared with the Vinton dome given that, while there are significant geochemical variations within individual cap rocks, domes along the Gulf Coast follow similar developmental patterns and compositional trends (Kyle and Posey, 1991; Walker, 1976). Given the shallow depth of the top of the cap rock at High Island (120 m), the density contrast between the caps and the lower density Quaternary sediments becomes dominant. In order to confirm the detection of the dome, an additional survey along the same traverse has been planned. This survey will be conducted using a CG-5 gravimeter.

4.2 Future Work

The development of a method to conduct airborne gravimetry using MEMS accelerometers is ongoing and a primary goal of the HELIX project. Airborne gravimetry could be useful on bodies such as Mars which have atmospheres that could support powered flight. Potential platforms include drones, balloons, and robotic helicopters such as the Ingenuity helicopter included in the Mars 2020 mission. As stated earlier, an airborne platform would allow some closure of the spatial scale gap between surface and orbital surveys in an efficient manner. It could also allow data to be collected over areas that are inaccessible by rovers or be valuable for studying crater fill in a relatively low-risk manner.

The fundamental problem in moving-base inertial gravimetry is the separation of gravity from kinematic accelerations. Given that inertial gravimetry is, in essence, a reversal of the

process used for determining kinematic accelerations in inertial navigation, many of the methods used in inertial navigation apply to inertial gravimetry.

4.2.1 Inertial Navigation

An INS is a three-dimensional dead-reckoning navigation system that incorporates triaxial accelerometers and gyroscopes as part of an IMU combined with a navigation processor. The navigation processor integrates the outputs of the accelerometers and gyroscopes to obtain position, velocity, and orientation information. The INS uses gravity models to obtain specific force measurements from which the kinematic acceleration of a vehicle is obtained. The integration of the kinematic acceleration gives the velocity solution, and the subsequent integration of velocity gives the position solution. These solutions are collectively known as the navigation solutions to the navigation equations used by the processor. The angular rate measurements output from the gyroscopes are integrated to give the orientation of the system.

As with moving-base gravimetry, the two mechanizations of INSs are strapdown and stabilized-platform. In the strapdown mechanization, the system is subject to the dynamics of the vehicle, which has an adverse effect on performance. However, a strapdown INS is small, lightweight, low cost, and easy to implement. The method under development is concerned with the strapdown mechanization.

4.2.2 Coordinate Frames

In order to describe positions on a surface, a system of coordinates is necessary. This holds true for planetary surfaces as well. Additionally, specific coordinate frames must be defined in which changes in motion, orientation, and position can be described. In navigation, a system of Cartesian coordinates with orthogonal axes, x, y, and z is defined in three-dimensional space. However, the defined axes can have various orientations in space. The sets of coordinate

axes define the coordinate frames. Coordinate frames can describe either a global or local frame of reference, which is dependent on the application. On Earth, the global frames are fixed to the Earth as it rotates or to stars that exhibit no relative motion, whereas the local frames are fixed to local directions.

The first frame to consider is the inertial frame (*i*-frame) – the coordinate system in which Newton's laws of motion are true. The inertial frame exhibits no rotation or acceleration with respect to the rest of the Universe. It is defined by the positions of stable quasars relative to the Earth and is Earth-centered (Jekeli, 2012). The *i*-frame is shown in figure 4.1.

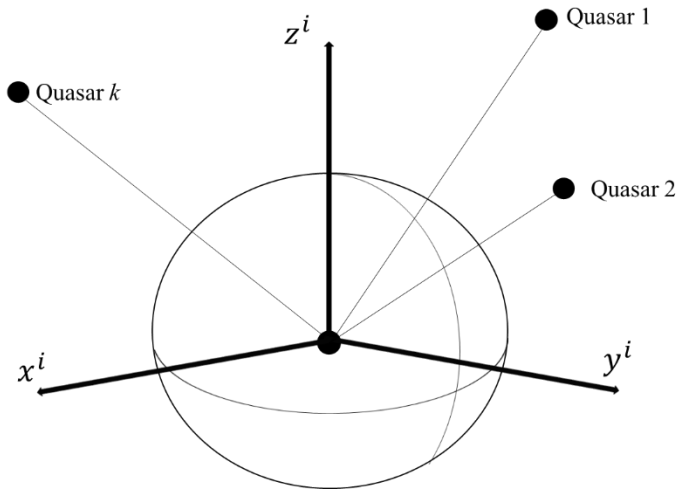

Figure 4.1 The Earth-Centered inertial frame.

The frame that is fixed to – and rotates with – the Earth is known as the Earth-Centered-Earth-Fixed frame (*e*-frame). The frame's origin is defined as the center of the ellipsoid, or approximately the Earth's center of mass. The z-axis is aligned with Earth's rotational axis, the y-axis is defined by the intersection between the equator and the 90° east meridian, and the x-axis is defined by the intersection between the equator and 0° longitude (Groves, 2013).

The last Earth-based frame considered in this study is the local navigation frame (*n*-frame). The frame in which the navigation equations are formulated. The frame is typically

defined by the local North-East-Down directions (Jekeli, 2012). The *n*-frame and *e*-frame are shown in figure 4.2.

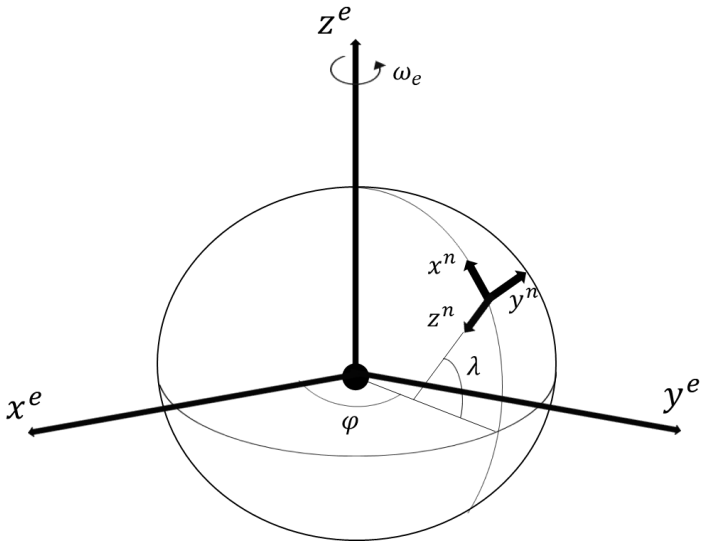

Figure 4.2. The Earth-Centered-Earth-Fixed frame with axes denoted by superscript e and local navigation frame with axes denoted by superscript n. ω_e is the rotation rate of the Earth, λ is latitude and φ is longitude.

In the strapdown configuration, an additional frame is used for the body of the carrier vehicle (*b*-frame) that defines the accelerometer axes relative to the vehicle. The x-axis points toward the front of the vehicle, the y-axis to the left of the vehicle, and the z-axis toward the bottom of the vehicle.

4.2.3 Orientation and Coordinate Transformations

The use of different coordinate frames naturally gives rise to relationships between each frame, which in turn gives rise to transformations between them. Assume C_t^s is a matrix that rotates coordinates in the vector x^t from the *t*-frame to the *s*-frame, then:

$$x^s = C_t^s x^t \tag{4.1}$$

The same operation can be performed on a matrix with the following modification: assume A^t is a matrix in the *t*-frame, then:

$$A^s = C_t^s A^t C_s^t \tag{4.2}$$

Orientations can be described using a sequence of rotations about different axes by angles known as Euler angles. The three rotations $R_{1,2,3}$, known as roll, γ, pitch, β, and yaw, α, can be combined into what is known as a direction cosine matrix (Jekeli, 2012):

$$R_3(\gamma)R_2(\beta)R_1(\alpha) = \begin{bmatrix} cos(\gamma)\,cos(\beta) & cos(\gamma)\,sin(\beta)\,sin(\alpha) + sin(\gamma)\,cos(\alpha) & -cos(\gamma)\,sin(\beta)\,cos(\alpha) + sin(\gamma)\,sin(\alpha) \\ -sin(\gamma)\,cos(\beta) & -sin(\gamma)\,sin(\beta)\,sin(\alpha) + cos(\gamma)\,cos(\alpha) & sin(\gamma)\,sin(\beta)\,cos(\alpha) + cos(\gamma)\,sin(\alpha) \\ sin(\beta) & -cos(\beta)\,sin(\alpha) & cos(\beta)\,cos(\alpha) \end{bmatrix} \tag{4.3}$$

Which can then be used as the transformation matrix C_t^s. Additionally, a rotation can be represented by quaternions. Quaternions are hyper-complex numbers consisting of four components:

$$q = [a, b, c, d] \tag{4.4}$$

where a represents the magnitude of the rotation and the following components represent the rotational axes (Groves, 2013). Quaternions can represent vectors in four dimensions just as complex numbers can represent vectors in two dimensions. Rotations of three-dimensional vectors by an angle, ζ, can also be represented by specific quaternions such as (Jekeli, 2012):

$$q_\zeta = cos\left(\frac{\zeta}{2}\right) + sin\left(\frac{\zeta}{2}\right)(bi + cj + dk) = a + bi + cj + dk \tag{4.5}$$

Then the quaternion vector is given by:

$$q = \left[cos\left(\frac{\zeta}{2}\right) \quad b\,sin\left(\frac{\zeta}{2}\right) \quad c\,sin\left(\frac{\zeta}{2}\right) \quad d\,sin\left(\frac{\zeta}{2}\right)\right]^T = [a \quad b \quad c \quad d]^T \tag{4.6}$$

Most navigation systems use quaternions since they are computationally efficient due to having only four components and being useful in the integration of angular rates (Groves, 2013). In order to use a rotation quaternion to perform coordinate transformations, its relationship to the

direction cosine matrix must be derived. Again, using the hypothetical frames related by C_t^s, this transformation can be described using an equivalent single rotation by ζ in the direction defined by the unit rotation vector, e_ζ^t, using spherical polar coordinates, θ, λ (Jekeli, 2012):

$$e_\zeta^t = \begin{bmatrix} b \\ c \\ d \end{bmatrix} = \begin{bmatrix} sin(\theta)\, cos(\lambda) \\ sin(\theta)\, sin(\lambda) \\ cos(\theta) \end{bmatrix} \tag{4.7}$$

A new frame, the ζ-frame, must be defined that represents the rotation in this direction. The transformation from the t-frame to the ζ-frame can be accomplished by:

$$C_t^\zeta = R_2(-\theta)R_3(-\pi + \lambda) = \begin{bmatrix} -cos(\theta)\, cos(\lambda) & cos(\theta)\, sin(\lambda) & sin(\theta) \\ sin(\lambda) & -cos(\lambda) & 0 \\ sin(\theta)\, cos(\lambda) & sin(\theta)\, sin(\lambda) & cos(\theta) \end{bmatrix} \tag{4.8}$$

The rotation about ζ in this frame is described by $R_3(\zeta)$. According to equation (4.2), the same rotation in the t-frame, which can be used as C_t^s, is given by:

$$C_t^s = C_\zeta^t R_3(\zeta) C_t^\zeta \tag{4.9}$$

The matrix C_t^ζ can be expressed in terms of the elements of the quaternion shown in equation (4.6) and using equation (4.7):

$$C_t^\zeta = \begin{bmatrix} \dfrac{-db}{\sqrt{1-d^2}} & \dfrac{-dc}{\sqrt{1-d^2}} & \sqrt{1-d^2} \\ \dfrac{c}{\sqrt{1-d^2}} & \dfrac{-b}{\sqrt{1-d^2}} & 0 \\ b & c & d \end{bmatrix} \tag{4.10}$$

From equation (4.7) and using the elements of equation (4.6) the transformation C_t^s can be expressed as:

$$C_t^s = \begin{bmatrix} a^2+b^2-c^2-d^2 & 2(bc+ad) & 2(bd-ac) \\ 2(bc-ad) & a^2-b^2+c^2-d^2 & 2(cd+ab) \\ 2(bd+ac) & 2(cd-ab) & a^2-b^2-c^2+d^2 \end{bmatrix} \tag{4.11}$$

Thus, demonstrating the relationship between quaternions and direction cosines.

In order to determine the transformation matrix from one frame to another, one must consider the fact that the relative orientation of the frames change with time due to movement. Thus, it is necessary to find the derivative of the transformation with respect to time. The derivative of the rotational transformation with respect to time is:

$$\dot{C}_t^s = \lim_{\delta\tau \to 0} \frac{C_t^s(\tau+\delta\tau) - C_t^s(\tau)}{\delta\tau} \tag{4.12}$$

The transformation that occurs at time $\tau + \delta\tau$ results from the transformation up to time τ accompanied by a small change of the s-frame relative to the t-frame during the interval of $\delta\tau$. This can be represented as:

$$C_t^s(\tau+\delta\tau) = \delta C^s C_t^s(\tau) \tag{4.13}$$

with:

$$\delta C^s = I - \Psi^s \tag{4.14}$$

where I is the identity matrix and Ψ is a skew symmetric matrix of small Euler angles:

$$\Psi = \begin{bmatrix} 0 & -\gamma & \beta \\ \gamma & 0 & -\alpha \\ -\beta & \alpha & 0 \end{bmatrix} \tag{4.15}$$

By substituting equations (4.13) and (4.14) into equation (4.12), the angular velocity of the s-frame relative to the t-frame with coordinates in the s-frame can be obtained:

$$\dot{C}_t^s = \lim_{\delta\tau \to 0} \frac{(I - \Psi^s)C_t^s(\tau) - C_t^s(\tau)}{\delta\tau}$$

$$= \lim_{\delta\tau \to 0} \frac{-\Psi^s C_t^s(\tau)}{\delta\tau} = -\lim_{\delta\tau \to 0} \frac{\Psi^s}{\delta\tau} C_t^s(\tau)$$

$$= -\Omega_{st}^s C_t^s \tag{4.16}$$

where Ω_{st}^s is a skew-symmetric matrix of angular rates:

$$\Omega_{st}^s = \begin{bmatrix} 0 & -\omega_3 & \omega_2 \\ \omega_3 & 0 & -\omega_1 \\ -\omega_2 & \omega_1 & 0 \end{bmatrix} \tag{4.17}$$

Using equation (4.2) and considering the relationship:

$$\Omega_{ts}^s = -\Omega_{st}^s \tag{4.18}$$

then:

$$\Omega_{ts}^s = -\Omega_{st}^s = -C_t^s \Omega_{st}^t C_s^t \tag{4.19}$$

Thus, the derivative of the transformation matrix with respect to time is:

$$\dot{C}_t^s = C_t^s \Omega_{st}^t \tag{4.20}$$

Using quaternions to solve the equation by substituting equation (4.11) into equation (4.20) yields the differential equation in terms of quaternions:

$$\dot{q} = \frac{1}{2} A q \tag{4.21}$$

with *A* being a skew-symmetric matrix of the time-dependent angular rates:

$$A = \begin{bmatrix} 0 & \omega_x & \omega_y & \omega_z \\ -\omega_x & 0 & \omega_z & -\omega_y \\ -\omega_y & -\omega_z & 0 & \omega_x \\ -\omega_z & \omega_y & -\omega_x & 0 \end{bmatrix} \tag{4.22}$$

with the angular rates being output from the gyroscopes, which sense the angular velocity of the *b*-frame relative to the *i*-frame:

$$\omega_{ib}^{i} = \begin{bmatrix} \omega_x \\ \omega_y \\ \omega_z \end{bmatrix} \tag{4.23}$$

The output from the gyroscopes represents angular increments per unit time. The angular increments from the gyroscopes are then given by:

$$\delta\theta_k = \int_{t_{k-1}}^{t_k} \omega_{ib}^{i} dt \tag{4.24}$$

The solution to equation (4.21) using gyroscope data is:

$$\hat{q}_k = \left(I + \frac{1}{2}\Theta_k + \frac{1}{8}\Theta_k^2 + \frac{1}{48}\Theta_k^3 + \cdots \right) \hat{q}_{k-1} \tag{4.25}$$

Where:

$$\Theta_k = \int_{t_{k-1}}^{t_k} A dt \tag{4.26}$$

In order to solve equation (4.25) an initialization procedure must be performed that gives the initial quaternion vector q_0. Then the equation becomes an iterative algorithm that solves for the subsequent quaternions q_k. One way to perform the initialization procedure is to use the initial Euler angles in a direction cosine matrix that describes the rotation from the *b*-frame to the *n*-frame:

$$C_b^n = \begin{bmatrix} cos(\alpha_0)\, cos(\beta_0) & cos(\alpha_0)\, sin(\beta_0)\, sin(\gamma_0) - sin(\alpha_0)\, cos(\gamma_0) & cos(\alpha_0)\, sin(\beta_0)\, cos(\gamma_0) + sin(\alpha_0)\, sin(\gamma_0) \\ sin(\alpha_0)\, cos(\beta_0) & sin(\alpha_0)\, sin(\beta_0)\, sin(\gamma_0) + cos(\alpha_0)\, cos(\gamma_0) & sin(\alpha_0)\, sin(\beta_0)\, cos(\gamma_0) - cos(\alpha_0)\, sin(\gamma_0) \\ -sin(\beta_0) & cos(\beta_0)\, sin(\gamma_0) & cos(\beta_0)\, cos(\gamma_0) \end{bmatrix} \tag{4.27}$$

the initial transformation matrix from the *b*-frame to the *i*-frame is then:

$$C_b^i = C_n^i C_b^n \tag{4.28}$$

with:

$$C_n^i = C_e^i C_n^e \tag{4.29}$$

$$C_e^i = \begin{bmatrix} cos(\omega_E t) & -sin(\omega_E t) & 0 \\ sin(\omega_E t) & cos(\omega_E t) & 0 \\ 0 & 0 & 1 \end{bmatrix} \tag{4.30}$$

$$C_e^n = \begin{bmatrix} -sin(\phi)\,cos(\lambda) & -sin(\lambda) & -cos(\phi)\,cos(\lambda) \\ -sin(\phi)\,sin(\lambda) & cos(\lambda) & -cos(\phi)\,sin(\lambda) \\ cos(\phi) & 0 & -sin(\phi) \end{bmatrix} \tag{4.31}$$

where ω_E is the mean rotation rate of the Earth and ϕ and λ are latitude and longitude, respectively. Then the initial quaternion can be found via (Jekeli, 2012):

$$a_0 = \frac{1}{2}\left(1 + C_{b_{1,1}}^i + C_{b_{2,2}}^i + C_{b_{3,3}}^i\right)^{\frac{1}{2}} \tag{4.32}$$

$$b_0 = \frac{1}{4a_0}\left(C_{b_{2,3}}^i - C_{b_{3,2}}^i\right) \tag{4.33}$$

$$c_0 = \frac{1}{4a_0}\left(C_{b_{3,1}}^i - C_{b_{1,3}}^i\right) \tag{4.34}$$

$$d_0 = \frac{1}{4a_0}\left(C_{b_{1,2}}^i - C_{b_{2,1}}^i\right) \tag{4.35}$$

4.2.4 Kalman Filter Approach

Both GPS and INS systems can provide position and velocity solutions, however, the differences in the solutions of each system will gradually increase over time due to systematic errors and drifts. Therefore, an integration algorithm that fuses information provided by each system should be applied in order to yield accurate solutions and estimates of the system errors. The most commonly used algorithm in inertial navigation and gravimetry is the Kalman filter. The Kalman filter is an optimal estimation algorithm that derives a minimum error estimate of the state of a system based on measurements, modeled system dynamics, and assumed statistics of the present noise processes (Kalman, 1960).

The standard Kalman filter operates as a best linear unbiased estimator when modeling linear systems. However, when modelling a non-linear system, such as the system under consideration, the extended Kalman filter (EKF) is used (Gelb, 1974). In inertial navigation and gravimetry, a common approach is to use the EKF to estimate the orientation of the INS along with the errors of the system (Glennie and Schwarz, 1999; Groves, 2013; Jekeli, 2012). For inertial gravimetry, the filter is sometimes augmented with modeled gravity disturbance estimates, though this method has produced mixed results (Kwon and Jekeli, 2001). The standard Kalman equations are as follows. Given an *n*-dimensional system state vector X_{k-1} at time t_{k-1}, the transition of the state to the next epoch t_k is:

$$X_k = F_k X_{k-1} + w_{k-1} \tag{4.36}$$

where F_k is the non-linear state transition matrix and w_{k-1} is a Gaussian white noise vector, also known as the system noise, such that $w \sim N(0, Q_k)$. Where Q_k is the system noise covariance matrix. Equation (2.36) can be linearized to give the discrete time form:

$$x_k = \Phi_{k-1} x_{k-1} + w_{k-1} \tag{4.37}$$

$$\Phi_{k-1} = I + F_{k-1} dt_{k-1} \tag{4.38}$$

The observability of the system is based on the concept of measurements, which are assumed to be linearly related to the system state via:

$$z_k = H_k X_k + v_k \tag{4.39}$$

where z_k are measurements, H_k is the observation matrix and, v_k is the measurement noise such that $v_k \sim N(0, R_k)$. Where R_k is the measurement noise covariance matrix. The filter is initialized with an initial state X_0 and state covariance matrix P_0. The filter then performs a two-step algorithm at every epoch. The first step is the prediction step, where the filter determines the

state transition from t_{k-1} to t_k. The second step is the measurement update, where the system state is filtered using the measurement z_k. The prediction is based on the estimates from the previous epoch:

$$\hat{X}_k^- = \Phi_{k-1}\hat{X}_{k-1} \tag{4.40}$$

$$\hat{P}_k^- = \Phi_{k-1}\hat{P}_{k-1}\Phi_{k-1}^T + Q_{k-1} \tag{4.41}$$

where X_k is the estimated state vector, X_k^- is the predicted state vector of the following epoch, P_k is the estimated state covariance matrix, and P_k^- is the predicted state covariance matrix. The update using measurements is performed via:

$$K_k = \hat{P}_k^- H_k^T \left(H_k \hat{P}_k^- H_k^T + R_k\right)^{-1} \tag{4.42}$$

$$\hat{X}_k = \hat{X}_k^- + K_k\left(z_k - H_k\hat{X}_k^-\right) \tag{4.43}$$

$$\hat{P}_k = (I - K_k H_k)\hat{P}_k^- \tag{4.44}$$

$$i_k = z_k - h\left(\hat{X}_k^-\right) \tag{4.45}$$

$$S_k = H_k \hat{P}_k^- H_k^T + R_k \tag{4.46}$$

where K_k is the Kalman gain, which defines the relative weight between the measurements and the current state estimate based on the system model. i_k is known as the innovation, which compares the true measurement with a hypothetical measurement $h\left(X_k^-\right)$, which represents an error-free sensor measurement. S_k is the innovation covariance matrix. The following subsections provide an overview of the construction of the Kalman Filter to be used in this project.

4.2.4.1 System State Propagation

The EKF used in this study includes a 15-dimensional state space given by:

$$X = [\Psi^i \ \delta\dot{x} \ \delta x^i \ \delta b_a^b \ \delta b_\omega^b]^T \tag{4.47}$$

where each component represents the 3-dimensional error in orientation Ψ^i, velocity $\delta\dot{x}^i$, and position δx^i in the inertial frame. δb_a^b and δb_ω^b are accelerometer and gyroscope biases in the IMU body frame. Notice that the accelerometer scale errors are not included as states. This is because the scale errors can propagate into the accelerometer bias estimates, assuming a relatively constant orientation throughout a survey (Becker, 2016). However, the filter can be augmented with an additional state to account for the scale error. This will be performed as needed. The state transition matrix is defined by the propagation of the states through time. Thus, the system model is composed of the time derivatives of the error dynamics equations of the system (Groves, 2013). Here, ^, denotes quantities which are estimated or calculated from estimates and, ~, denotes quantities indicated by the INS.

From equation (4.15), the attitude error is defined by small Euler angles thus, by taking the derivative of its transformation matrix counterpart, the attitude error propagation can be obtained which, after simplification, is dependent on the gyroscope errors:

$$\delta\Psi^i \approx \hat{C}_b^i \delta\omega_{ib}^b = \hat{C}_b^i b_g \tag{4.48}$$

The propagation of the velocity error is dependent on the specific force:

$$\delta\dot{x}^i = \tilde{f}^i - f^i + \tilde{g}^i - g^i \tag{4.49}$$

Since the specific force is measured in the body frame, it is dependent on both the accelerometer errors and attitude errors:

$$\tilde{f}^i - f^i = \tilde{C}_b^i \tilde{f}^b - C_b^i f^b \tag{4.50}$$

$$\tilde{f}^i - f^i \approx \hat{C}_b^i \left(\tilde{f}^i - f^i\right) + \left(\tilde{C}_b^i - C_b^i\right)\hat{f}^b \tag{4.51}$$

The error in the specific force is given by equation (1.9), however, since only the accelerometer bias is modeled in the filter, the specific force error becomes:

$$\tilde{f}^i - f^i = \delta f^b \approx b_a \tag{4.52}$$

Then, an attitude error approximation can be applied by using a rearranged version of equation (4.14):

$$\tilde{C}_b^i - C_b^i = \left(\delta C_b^i - I\right) C_b^i \approx C_b^i \Omega_{ib}^i \tag{4.53}$$

The gravity term in equation (4.49) can be approximated using:

$$\tilde{g}^i - g^i \approx \frac{2g_0\left(\hat{\lambda}_b\right)}{r_{eS}^e\left(\hat{\lambda}_b\right)} \frac{\hat{x}^i}{|\hat{x}^i|^2} \hat{x}^{i^T} \delta x^i \tag{4.54}$$

where g_0 is the normal gravity minus centripetal acceleration, λ_b is geodetic longitude, and r_{eS}^e is the geocentric radius at a given point on the Earth's surface. The time derivative of the velocity error is then obtained by substituting equations (4.52) and (4.53) into equation (4.51), and equations (4.51) and (4.54) into equation (4.48):

$$\delta \dot{x}^i = [-\left(\hat{C}_b^i \hat{f}^b\right) \times] \delta \Psi^i + \frac{2g_0\left(\hat{\lambda}_b\right)}{r_{eS}^e\left(\hat{\lambda}_b\right)} \frac{\hat{x}^i}{|\hat{x}^i|^2} \hat{x}^{i^T} \delta x^i + \hat{C}_b^i b_a \tag{4.55}$$

The position error propagation in the *i*-frame is equal to the velocity error, thus:

$$\delta \dot{x}^i = \delta v^i \tag{4.56}$$

The sensor biases are modeled as random constants with unknown variances:

$$\dot{b}_a = 0, \dot{b}_g = 0 \tag{4.57}$$

The state transition matrix is then constructed as (Groves, 2013):

$$\Phi^i = \begin{bmatrix} I_{3\times3} & 0_{3\times3} & 0_{3\times3} & 0_{3\times3} & \hat{C}_b^i t_k \\ F_{21}^i t_k & I_{3\times3} & F_{23}^i t_k & \hat{C}_b^i t_k & 0_{3\times3} \\ 0_{3\times3} & I t_k & I_{3\times3} & 0_{3\times3} & 0_{3\times3} \\ 0_{3\times3} & 0_{3\times3} & 0_{3\times3} & I_{3\times3} & 0_{3\times3} \\ 0_{3\times3} & 0_{3\times3} & 0_{3\times3} & 0_{3\times3} & I_{3\times3} \end{bmatrix} \tag{4.58}$$

where

$$F_{21}^i = \left[-\left(\hat{C}_b^i \hat{f}^b\right) \times\right] \tag{4.59}$$

$$F_{23}^{i} = \frac{2g_0(\hat{\lambda}_b)}{r_{eS}^{e}(\hat{\lambda}_b)} \frac{\hat{x}^i}{|\hat{x}^i|^2} \hat{x}^{i^T} \tag{4.60}$$

4.2.4.2 System Noise

The noise covariance matrix is constructed using the noise characteristics of the inertial sensors (Groves, 2013):

$$Q_k = \begin{bmatrix} \eta_{rg}^2 I_{3\times3} & 0_{3\times3} & 0_{3\times3} & 0_{3\times3} & 0_{3\times3} \\ 0_{3\times3} & \eta_{ra}^2 I_{3\times3} & 0_{3\times3} & 0_{3\times3} & 0_{3\times3} \\ 0_{3\times3} & 0_{3\times3} & 0_{3\times3} & 0_{3\times3} & 0_{3\times3} \\ 0_{3\times3} & 0_{3\times3} & 0_{3\times3} & \eta_{bia}^2 I_{3\times3} & 0_{3\times3} \\ 0_{3\times3} & 0_{3\times3} & 0_{3\times3} & 0_{3\times3} & \eta_{big}^2 I_{3\times3} \end{bmatrix} \tag{4.61}$$

where, η_{rg}^2 and η_{ra}^2 are gyroscope and accelerometer random noise and, η_{bia}^2 and η_{big}^2 are the bias instabilities of the accelerometers and gyroscopes, respectively. In this study, these parameters are determined using a method known as Allan Variance, which is designed to study the frequency stability of precision oscillators. The Allan Variance of a dataset is defined as half the time average of the squares of the differences between successive frequency deviations, y, over a sampling period, τ (Allan, 1966):

$$\sigma_y^2(\tau) = \frac{1}{2}\langle (y_{n+1} - y_n)^2 \rangle \tag{4.62}$$

The Allan Deviation, defined as the square root of the Allan Variance, provides the necessary information to analyze the noise characteristics of a device (Allan, 1966):

$$\sigma_y(\tau) = \sqrt{\sigma_y^2(\tau)} \tag{4.63}$$

Since the Allan Deviation is directly measurable, the noise parameters can be obtained directly from a log-log plot of the Allan Deviation over the sampling period. The parameters of interest are the accelerometer and gyroscope random walks and bias instabilities. The integral solutions for these parameters are given by (El-Sheimy et. al., 2008):

$$\sigma^2(\tau) = \frac{N^2}{\tau} \tag{4.64}$$

$$\sigma^2(\tau) = \frac{2B^2}{\pi}[ln\,2 - \frac{sin^3\,x}{2x^2}(sin\,x + 4x\,cos\,x) + C_i(2x) - C_i(4x)] \tag{4.65}$$

$$x = \pi f_0 \tau \tag{4.66}$$

where N is the random walk coefficient, B is the bias instability coefficient, C_i is the cosine-integral function, and f_0 is the cutoff frequency. Detailed overviews can be found in Tehrani (1983), IEEE (1998), IEEE (1999), and El-Sheimy et. al. (2008). On a log-log plot of the Allan Deviation, the random walks of the sensors occur at a slope of -0.5 and the bias instabilities at a slope of 0 (El-Sheimy et. al., 2008). Allan deviation curves for 1 Hz data from the HELIX accelerometers and gyroscopes are shown in figures 4.3 and 4.4. The noise characteristics identified from these plots are shown in table 4.1.

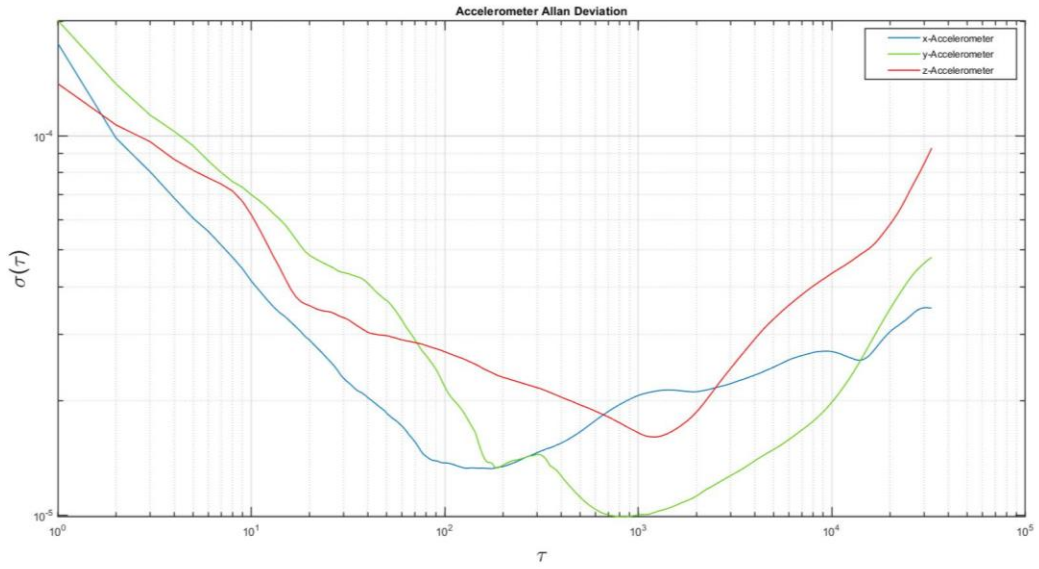

Figure 4.3. Accelerometer Allan deviation.

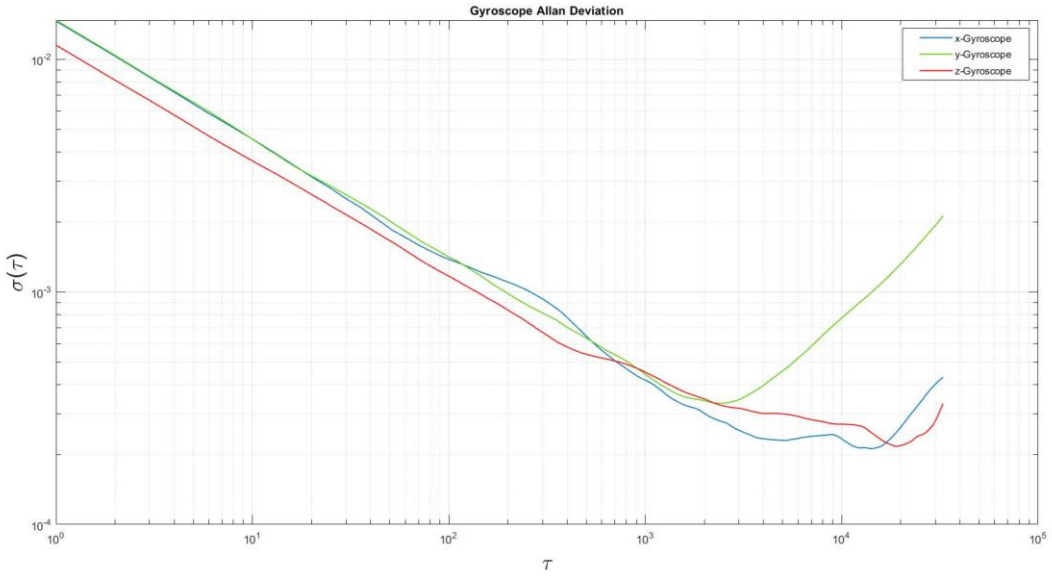

Figure 4.4. Gyroscope Allan deviation.

Table 4.1. IMU Noise Characteristics

Axis	**Accelerometer Random Noise**	**Accelerometer Bias Instability**	**Gyroscope Random Noise**	**Gyroscope Bias Instability**
x	19.7 mgal	1.33 mgal	4.35×10^{-4} ° s^{-1}	2.14×10^{-4} ° h^{-1}
y	13.3 mgal	2.08 mgal	4.78×10^{-4} ° s^{-1}	2.81×10^{-4} ° h^{-1}
z	31.4 mgal	2.12 mgal	1.90×10^{-3} ° s^{-1}	2.31×10^{-4} ° h^{-1}

4.2.4.3 Measurements

The measurements used to filter the system state are defined as the differences between the measurements of the GPS and INS (Groves, 2013). The measurement vector, z_k is then:

$$z_k = \begin{bmatrix} \delta x^i \\ \delta \dot{x}^i \end{bmatrix} = \begin{bmatrix} x^i_{INS} - x^i_{GPS} \\ \dot{x}^i_{INS} - \dot{x}^i_{GPS} \end{bmatrix}_k \tag{4.67}$$

The observation matrix is (Groves, 2013):

$$H = \begin{bmatrix} 0_{3\times3} & 0_{3\times3} & -I_{3\times3} & 0_{3\times3} & 0_{3\times3} \\ 0_{3\times3} & -I_{3\times3} & 0_{3\times3} & 0_{3\times3} & 0_{3\times3} \end{bmatrix} \tag{4.68}$$

Finally, the measurement noise covariance matrix is composed of the standard deviations of the GPS position and velocity measurements:

$$R_k = \begin{bmatrix} \sigma_x^2 I_{3\times3} & 0_{3\times3} \\ 0_{3\times3} & \sigma_{\dot{x}}^2 I_{3\times3} \end{bmatrix}_k \tag{4.69}$$

4.3 Conclusion

To the author's knowledge, the results of the High Island field test would represent the first detection of a subsurface structure using an IMU, if confirmed. This finding would further demonstrate the potential of MEMS devices for use in gravimetry. It could additionally serve as a proof of concept for instrumentation included in future NASA missions. The integration of MEMS devices into planetary exploration would constitute reductions in cost, mass, power requirements, and risks given their robustness. Additionally, by combining a triad of gravimeter-qualifying MEMS accelerometers with precision rate gyroscopes, instruments that serve both scientific and engineering/navigation purposes could be integrated into future instrument suites, further reducing cost, mass, and power requirements.

The findings of this thesis have direct implications for proposals currently under development such as the GEMMA instrument and the Intrepid Lunar rover. A MEMS IMU is currently planned to be integrated into the Intrepid instrument suite to measure subsurface density (Robinson et. al., 2020). The IMU is the LN-200s, which has a precision comparable to

the IMU-3030 used in this study. The drifts and calibration procedures identified in this thesis have direct applicability to the development of the Intrepid mission.

Additionally, the importance of mitigating the effect of temperature variations were further confirmed. Future MEMS gravimetric instruments for planetary exploration would benefit enormously from a temperature stabilization system, which should be a major focus of future development. It could be feasible to develop internal temperature stabilization systems for such devices, though given the small size of MEMs instruments, an external thermally stabilized housing should be viable as well.

Airborne-based planetary gravimetry could allow higher resolution gravity data to be collected at a rate that is currently unprecedented. Eventually, multiple small robotic aircraft could work in unison, surveying large portions of planetary surfaces. Near-term development of prototype platforms should focus on the following:

1.) Determining the most effective airborne platforms, e.g. fixed-wing drones, rotorcraft, balloons, etc. Initially, such a determination should be based on robustness to turbulence, endurance, and maximum payload.
2.) Mitigating thermal drifts due to the instrument being exposed to large temperature variations given that such small aircraft will likely have no temperature regulation system available.
3.) Considering the effect of significant orientation changes due to changes in wind direction and speed.

Moving data was collected over the salt dome and will be subjected to the methods described in the future work section of this thesis. If the same precision is achieved in the moving datasets, it would constitute the first successful moving-base inertial gravimetry survey

conducted using a MEMS device, again, to the author's knowledge. Additionally, it would likely help initiate the development of airborne platforms for planetary gravimetry, which would be an additional paradigm shift for planetary exploration.

REFERENCES

Allan, D. W. (1966). Statistics of Atomic Frequency Standards. Proceedings of the IEEE. https://doi.org/10.1109/PROC.1966.4634

Anthony, J. W., Bideaux, R. A., Bladh, K. W., & Nichols., M. C. (2003). Handbook of Mineralogy. Mineralogical Society of America.

Ayres-Sampaio, D., Deurloo, R., Bos, M., Magalhães, A., & Bastos, L. (2015). A Comparison Between Three IMUs for Strapdown Airborne Gravimetry. Surveys in Geophysics. https://doi.org/10.1007/s10712-015-9323-5

Baker, E. T. J. (1995). Stratigraphic Nomenclature and Geologic Sections of the Gulf. U.S. Geological Survey Open-File Report.

Becker, D. (2016). Advanced calibration methods for strapdown airborne gravimetry (No. 51). Technische Universität Darmstadt.

Becker, D., Nielsen, J. E., Ayres-Sampaio, D., Forsberg, R., Becker, M., & Bastos, L. (2015). Drift reduction in strapdown airborne gravimetry using a simple thermal correction. Journal of Geodesy. https://doi.org/10.1007/s00190-015-0839-8

Blakely, R. J. (1995). Potential theory in gravity and magnetic applications. Cambridge university press.

Bruton, A. M., Schwarz, K.-P., & Škaloud, J. (2000). The use of wavelets for the analysis and de-noising of kinematic geodetic measurements. https://doi.org/10.1007/978-3-642-59742-8_37

Donoho, D. L. (1995). De-Noising by Soft-Thresholding. IEEE Transactions on Information Theory. https://doi.org/10.1109/18.382009

Donoho, D. L., & Johnstone, J. M. (1994). Ideal spatial adaptation by wavelet shrinkage. Biometrika. https://doi.org/10.1093/biomet/81.3.425

Drinkwater, M. R., Floberghagen, R., Haagmans, R., Muzi, D., & Popescu, A. (2003). GOCE:

ESA's first earth explorer core mission. Space Science Reviews. https://doi.org/10.1023/A:1026104216284

El-Sheimy, N., Hou, H., & Niu, X. (2008). Analysis and modeling of inertial sensors using Allan variance. IEEE Transactions on Instrumentation and Measurement. https://doi.org/10.1109/TIM.2007.908635

Ennen, C., & Hall, S. (2011). Structural mapping of the Vinton salt dome, Louisiana, using gravity gradiometry data. Society of Exploration Geophysicists International Exposition and 81st Annual Meeting 2011, SEG 2011.

Farrell, J. A., Silva, F. O., Rahman, F., & Wendel, J. (2019). IMU error state modeling for state estimation and sensor calibration: a tutorial. IEEE.

Gelb, A. (1974). Applied optimal estimation, MIT press.

Glennie, C., & Schwarz, K. P. (1999). A comparison and analysis of airborne gravimetry results from two strapdown inertial/DGPS systems. Journal of Geodesy. https://doi.org/10.1007/s001900050248

Hirt, C., Claessens, S. J., Kuhn, M., & Featherstone, W. E. (2012). Kilometer-resolution gravity field of Mars: MGM2011. Planetary and Space Science. https://doi.org/10.1016/j.pss.2012.02.006

Hwang, C., Hsiao, Y. S., & Shih, H. C. (2006). Data reduction in scalar airborne gravimetry: Theory, software and case study in Taiwan. Computers and Geosciences. https://doi.org/10.1016/j.cageo.2006.02.015

IEEE Standard Specification Format Guide and Test Procedure for Single-Axis Interferometric Fiber Optic Gyros, in IEEE Std 952-1997 , vol., no., pp.1-84, 24 Feb. 1998.

IEEE Standard Specification Format Guide and Test Procedure for Linear, Single-Axis, Non-Gyroscopic Accelerometers, IEEE Std. 1293-1998, 1999.

Jackson, M. P. A., & Talbot, C. J. (1986). External shapes, strain rates, and dynamics of salt structures. Geological Society of America Bulletin. https://doi.org/10.1130/0016-7606(1986)97

Jackson, M. P. A., Vendeville, B. C., & Shultz-Ela, D. D. (1994). Structural dynamics of salt systems. Annual Review of Earth and Planetary Sciences. https://doi.org/10.1146/annurev.ea.22.050194.000521

Jekeli, C. (2012). Inertial navigation systems with geodetic applications. In Inertial Navigation Systems with Geodetic Applications. https://doi.org/10.1515/9783110800234

Jenkins, A. J., Messfin, D., & Moon, W. (1983). Gravity modelling of salt domes and pinnacle reefs. J. Can. Soc. Explor. Geophys, 19(1), 51-56.

Jolliffe, I. T. (1986). Principal components in regression analysis. Springer, New York, NY.

Kalman, R. E. (1960). A New Approach to Linear Filtering and Prediction Problems. ASME. J. Basic Eng. 82(1): 35–45. https://doi.org/10.1115/1.3662552

Kwon, J. H., & Jekeli, C. (2001). A new approach for airborne vector gravimetry using GPS/INS. Journal of Geodesy. https://doi.org/10.1007/s001900000130

Kyle, J. R., & Posey, H. H. (1991). Halokinesis, cap rock development, and salt dome mineral resources. In *Developments in sedimentology* (Vol. 50, pp. 413-474). Elsevier.

Lewis, K. W., Peters, S., Gonter, K., Morrison, S., Schmerr, N., Vasavada, A. R., & Gabriel, T. (2019). A surface gravity traverse on Mars indicates low bedrock density at Gale crater. Science. https://doi.org/10.1126/science.aat0738

Lewis, K. W., Schmerr, N. C., Seshia, A. A., Niles, P. B., Sotzen, J. P. (2019) GEMMA: Geophysical Exploration of the Moon with MEMS Accelerometers. AGU Fall Meeting, P31C-3451.

Lewis, K. W., Schmerr, N. C., Seshia, A. A., Niles, P. B., Sotzen, J. P. (2020) The Future of Planetary Surface Gravimetry. AGU Fall Meeting, P081-0002.

Li, X., & Jekeli, C. (2008). Ground-vehicle INS/GPS vector gravimetry. Geophysics. https://doi.org/10.1190/1.2821155

Lötters, J. C., Schipper, J., Veltink, P. H., Olthuis, W., & Bergveld, P. (1998). Procedure for in-use calibration of triaxial accelerometers in medical applications. Sensors and Actuators, A: Physical. https://doi.org/10.1016/S0924-4247(98)00049-1

Lowrie, W. (2007). Fundamentals of Geophysics, second edition. In Cambridge University Press.

MEMSense. (2019). MS-IMU3030 Inertial Measurement Unit Product Specification. https://www.memsense.com/assets/docs/uploads/ms-imu3030/MS-IMU3030_PSUG.pdf

Michel T. Halbouty. (1936). Geology and Geophysics Showing Cap Rock and Salt Overhang of High Island Dome, Galveston County, Texas. AAPG Bulletin. https://doi.org/10.1306/3d932dda-16b1-11d7-8645000102c1865d

Middlemiss, R. P., Samarelli, A., Paul, D. J., Hough, J., Rowan, S., & Hammond, G. D. (2016). Measurement of the Earth tides with a MEMS gravimeter. Nature. https://doi.org/10.1038/nature17397

Murray, G., 1961, Geology of the Atlantic and Gulf Coastal Province of North America. New York: Harper and Brothers.

Mustafazade, A., Pandit, M., Zhao, C., Sobreviela, G., Du, Z., Steinmann, P., Zou, X., Howe, R. T., & Seshia, A. A. (2020). A vibrating beam MEMS accelerometer for gravity and seismic measurements. Scientific Reports. https://doi.org/10.1038/s41598-020-67046-x

Robinson, M., Elliot, J., Intrepid Science Team, NASA JPL. (2020). Intrepid Planetary Mission Concept Study Report. NASA Jet Propulsion Laboratory.

Nassar, S., & El-Sheimy, N. (2005). Wavelet analysis for improving INS and INS/DGPS navigation accuracy. Journal of Navigation. https://doi.org/10.1017/S0373463304003005

Newton, I. (1687). Philosophiae naturalis principia mathematica. In Philosophiae naturalis principia mathematica. https://doi.org/10.5479/sil.52126.39088015628399

Niebauer, T. (2015). Gravimetric Methods - Absolute and Relative Gravity Meter: Instruments Concepts and Implementation. In Treatise on Geophysics: Second Edition. https://doi.org/10.1016/B978-0-444-53802-4.00057-9

NOAA. (2021). CO-OPS Meteorological Observations. https://tidesandcurrents.noaa.gov/met.html?id=8770808

Ramberg, I. B., & Lind, G. (1968). Gravity measurements on the Paarup salt dome. *Meddelelser*

fra Dansk Geolog. Forening, *18*(2).

Reigber, C., Lühr, H., & Schwintzer, P. (2002). CHAMP mission status. Advances in Space Research. https://doi.org/10.1016/S0273-1177(02)00276-4

Talbot, C. J. (1993). Spreading of salt structures in the Gulf of Mexico. Tectonophysics. https://doi.org/10.1016/0040-1951(93)90338-K

Tang, S., Liu, H., Yan, S., Xu, X., Wu, W., Fan, J., Liu, J., Hu, C., & Tu, L. (2019). A high-sensitivity MEMS gravimeter with a large dynamic range. Microsystems and Nanoengineering. https://doi.org/10.1038/s41378-019-0089-7

Tapley, B. D., Bettadpur, S., Ries, J. C., Thompson, P. F., & Watkins, M. M. (2004). GRACE measurements of mass variability in the Earth system. *Science*, *305*(5683), 503-505.

Tehrani, M. M. (1983). Ring Laser Gyro Data Analysis With Cluster Sampling Technique. Fiber Optic and Laser Sensors I. https://doi.org/10.1117/12.935818

Titterton, D., & Weston, J. (2004). Strapdown Inertial Navigation Technology. In Strapdown Inertial Navigation Technology. https://doi.org/10.1049/pbra017e

Walker, C. W. (1976). Origin of Gulf Coast salt-dome cap rock. *AAPG Bulletin*, *60*(12), 2162-2166.

Watanabe, H., Yamada, N., & Okaji, M. (2004). Linear thermal expansion coefficient of silicon from 293 to 1000 K. International Journal of Thermophysics. https://doi.org/10.1023/B:IJOT.0000022336.83719.43

Wei, M., & Schwarz, K. P. (1998). Flight test results from a strapdown airborne gravity system. Journal of Geodesy. https://doi.org/10.1007/s001900050171

Wise, K. D. (2007). Integrated sensors, MEMS, and microsystems: Reflections on a fantastic voyage. In Sensors and Actuators, A: Physical. https://doi.org/10.1016/j.sna.2007.02.013

Zuber, M. T., Smith, D. E., Watkins, M. M., Asmar, S. W., Konopliv, A. S., Lemoine, F. G., Melosh, H. J., Neumann, G. A., Phillips, R. J., Solomon, S. C., Wieczorek, M. A., Williams, J. G., Goossens, S. J., Kruizinga, G., Mazarico, E., Park, R. S., & Yuan, D. N. (2013). Gravity field of the moon from the Gravity Recovery and Interior Laboratory

(GRAIL) mission. Science. https://doi.org/10.1126/science.1231507